PHYSICAL ASPECTS OF CHEMOTAXIS AND PROLIFERATION OF DICTYOSTELIUM DISCOIDEUM AMOEBA

A Dissertation

Presented to the Faculty of the Graduate School

of Cornell University

in Partial Fulfillment of the Requirements for the Degree of

Doctor of Philosophy

by

Igor Šegota

August 2014

PHYSICAL ASPECTS OF CHEMOTAXIS AND PROLIFERATION OF DICTYOSTELIUM DISCOIDEUM AMOEBA

Igor Šegota, Ph.D.

Cornell University 2014

In this dissertation, we explore two aspects of *Dictyostelium discoideum* life cycle, chemotaxis and proliferation. We use Shannon's information theory to study the physical limits of chemotaxis due to the stochastic process of ligands binding and unbinding to cell receptors (receptor noise). Using microfluidic experiments, we show that cells acquire much more information than the contemporary application of this theory allows. Next, we investigate how cells modify their extracellular environment by secreting enzymes that degrade chemoattractants and show that simple first order degradation leads to the significant improvement of the receptor signal-to-noise ratio of chemical gradients. Finally, we investigate the seemingly solitary vegetative phase of the same cells and find that they synchronize their growth after transferring from suspension culture to substrate. We show that this synchronization can be suppressed using microfluidic flow experiments, indicating that the synchronization is a collective behavior mediated by a diffusible molecule.

BIOGRAPHICAL SKETCH

Igor Šegota was born in Zagreb, Croatia in July 1982. He received a Dipl.ing. degree (an equivalent of Bachelors of Science) in Physics from University of Zagreb, Croatia with a thesis ”Loschmidt Echo of a 1D Boson Gas” advised by Prof. H. Buljan. Shortly after, he began graduate studies at Cornell University, Department of Physics.

ACKNOWLEDGEMENTS

I thank my adviser Prof. Carl Franck for his guidance during the last several years and for teaching me part of his experimental physicist's toolkit. I have also much benefited and I am grateful for our continuous discussions which resulted in greatly improved science and manuscripts. Finally, I am grateful for the freedom in choosing and pursuing my own scientific projects.

I thank the undergraduate students Ariana Standburg-Peshkin, Archana Rachankonda, Laurent Boulet, Kevin Tharratt for assistance with experiments.

I thank Dr. Theresa Porri, Prof. Mingming Wu for sharing their expertise and guiding me through and instructing me in microfluidic techniques and techniques of cell biology. I thank Prof. Eberhard Bodenschatz for equipment and support.

I also thank my committee members Prof. Veit Elser, Prof. Sol Gruner and Prof. Eric Siggia for insightful comments and suggestions.

The first year of this work was funded by National Institutes of Health grant (P01 GM078586) while the remaining time was supported through the Cornell Physics Department teaching assistanships. I much appreciate the efforts of John Miner, Professors Seamus Davis and Andre LeClair for the opportunity in lecturing.

TABLE OF CONTENTS

LIST OF TABLES

LIST OF FIGURES

CHAPTER 1

INTRODUCTION

It has been long known that living cells can respond to and move along chemical gradients. The first theme of this work is the motion of individual living eukaryotic cells in response to spatial chemical gradients, the process of chemotaxis. Chemotaxis is now well understood in bacteria where these cells are able to measure spatial chemical gradients by converting them into temporal gradients by moving and comparing how the chemical concentration varies with time [1]. In contrast, chemotaxis in eukaryotic cells is fundamentally different. They are large enough that they are able to measure the chemical gradients directly by performing snapshots of the spatial distribution of the occupied receptors on their surface to which chemicals can bind. In addition, the signaling pathways of genes and proteins inside the cells are far more complicated and it is our attempt to achieve a better quantitative understanding of this complicated process.

The model organism used in this work is the eukaryote *Dictyostelium discoideum* amoeba. These amoebae are believed to live their lives as single cells in their vegetative state, feeding on bacteria. Bacteria-secreted folic acid serves as a chemoattractant. When the food supply runs out, *D. discoideum* start their developmental program where they aggregate together into groups of 10^4 to 10^6 cells, forming a slime mold and eventually differentiating into the stalk and spore cells able to whitstand much harsher conditions [2]. The aggregation is mediated by non-dissipating waves of cyclic-adenosine-monophosphate (cAMP) which is secreted by cells and serves as another chemoattractant [2].

The physical limits of sensing chemical concentrations and gradients have

been extensively studied [3-14]. The common theme of these studies is to theoretically calculate the physical limit of sensing and then compare it with the experiments. Recently, in *D. discoideum* cAMP chemotaxis, Fuller et al.[9] employed Shannon's information theory and found that the mutual information between the gradient direction and the joint state of the occupied receptors ("external" mutual information) is close to the mutual information between the gradient direction and the angular distribution of the cell response for shallow gradients and low concentrations. This implies that the receptor noise in this regime dominates the entire noise in the chemotaxis process. A consequence of their result is that the external mutual information per receptor is independent of any physical or biochemical parameters if the cAMP concentrations are scaled by cAMP/cAMP receptor dissociation constant K_d and the cAMP gradients by K_d/R where R is the cell radius (i.e. external mutual information is implied to follow a universal law). However, in contrast to cAMP, folic acid chemotaxis occurs with much higher fidelity than allowed by the data-processing inequality (total mutual information is larger than the external) and is a focus of study in Chapter 1 of this thesis.

Many eukaryotic cells are also known to secrete enzymes that degrade their chemoattractants [2,15-18] but it is currently not clear how or even whether these enzymes significantly affect the chemoattractant gradient in the vicinity of the cell. With the advent of flow microfluidic devices where gradients are established by flow that is transverse to the gradient, the natural signal processing between the cell-secreted enzymes and cAMP is destroyed. The Chapter 2 theoretically examines the effect the secreted enzyme cAMP phosphodiesterase (PDE) has on the cAMP gradients perceived by cells. Our results imply that the local gradient around cells can be significantly altered in this way.

It is generally believed that *D. discoideum* cells transition from vegetative solitary to collective behavior only during their starvation phase [2]. In Chapter 3, we reveal that proliferation kinetics in the vegetative phase yielded a genuine surprise [19], after cells are transferred from suspension to surface culture.

1. V. Sourjik and N.S. Wingreen, "Responding to chemical gradients: bacterial chemotaxis", Curr. Opin. Cell Biol., 24, pp.262-268 (2012)
2. R.H. Kessin, "Dictyostelium: Evolution, Cell Biology and the Development of Multicellularity", Cambridge University Press, Cambridge (2001)
3. H.C. Berg and E.M. Purcell, "Physics of chemoreception", Biophys. J., 20, pp.193-215 (1977)
4. R.G. Endres and N.S. Wingreen, "Accuracy of direct gradient sensing by single cells", PNAS, 105, pp.15749-15754 (2008)
5. T. Mora and N.S. Wingreen, "Limits of Sensing Temporal Concentration Changes by Single Cells", Phys. Rev. Lett., 104, 248101 (2010)
6. B. Hu, W. Chen, J-W. Rappel and H. Levine, "Physical Limits on Cellular Sensing of Spatial Gradients", Phys. Rev. Lett., 105, 048104 (2010)
7. W-J. Rappel and H. Levine, "Receptor noise limitations on chemotactic sensing", PNAS, 105, pp.19270-19275 (2008)
8. B. Hu, W. Chen, H. Levine and W-J. Rappel, "Quantify- ing information transmission in eukaryotic gradient sensing and chemotactic response", J. Stat. Phys., 142, pp.1167- 1186 (2011)
9. D. Fuller, W. Chen, M. Adler, A. Groisman, H. Levine, W- J. Rappel and W.F. Loomis, "External and internal con- straints on eukaryotic chemotaxis", PNAS, 107, pp.9656- 9659 (2010)

10. M. Ueda and T. Shibata, "Stochastic Signal Processing and Transduction in Chemotactic Response of Eukaryotic Cells", Biophys. J., 93, pp.11-20 (2007)

11. L. Song, S.M. Nadkarni, H.U. Bodeker, C. Beta, A. Bae, C. Franck, W-J. Rappel, W.F. Loomis and E. Bodenschatz, "Dictyostelium discoideum chemotaxis: threshold for di- rected motion", Eur. J. Cell Biol., 85, pp.981-989 (2006)

12. G. Amselem, M. Theves, A. Bae, C. Beta and E. Bo- denschatz, "Control parameter description of eukaryotic chemotaxis", Phys. Rev. Lett., 109, 108103 (2012)

13. G. Amselem, M. Theves, A. Bae, E. Bodenschatz and C. Beta, "A stochastic description of Dictyostelium chemotaxis", PLoS One,7(5):e37213 (2012)

14. I. Segota, S. Mong, E. Neidich, A. Rachakonda, C. J. Lussenhop and C. Franck, High fidelity information processing in folic acid chemotaxis of Dictyostelium amoebae", J. R. Soc. Interface, 10, 20130606 (2013)

15. S.H. Zigmond. "Ability of polymorphonuclear leukocytes to orient in gradients of chemotactic factors." J. Cell. Biol. 75:606-616 (1977)

16. N. Barkai, M.D. Rose, N. Wingreen. ?Protease helps yeast find mating partners" Nature 396:422-423 (1998)

17. S.S. Andrews, N.J. Addy, R. Brent, A.P. Arkin. "Detailed Simulations of Cell Biology with Smoldyn 2.1", PLoS Comp. Biol. 6:e1000705 (2010)

18. M. Jin, B. Errede, M. Behar, W. Mather, S. Nayak, J. Hasty, H.G. Dohlman, T.C. Elston. "Yeast Dynamically Modify Their Environment to Achieve Better Mating Efficiency" Science Signaling 4: ra54 (2011)

19. I. Segota, L. Boulet, D. Franck and C. Franck, “Spontaneous emergence of large scale cell cycle synchronization in amoeba colonies” Phys Biol. 11(3):036001 (2014)

Chapter 2

High fidelity information processing in folic acid chemotaxis of Dictyostelium amoebae

Igor Segota, Surin Mong, Eitan Neidich, Archana Rachakonda,

Catherine J. Lussenhop and Carl Franck

J. Roy. Soc. Interface, 10, 88: 20130606 (2013)

Abstract

Living cells depend upon the detection of chemical signals for their existence. Eukaryotic cells can sense a concentration difference as low as a few percent across their bodies. This process was previously suggested to be limited by the receptor-ligand binding fluctuations. Here, we first determine the chemotaxis response of *Dictyostelium* cells to static folic acid gradients and show that they can significantly exceed this sensitivity, responding to gradients as shallow as 0.2% across the cell body. Second, using a previously developed information theory

framework, we compare the total information gained about the gradient (based on the cell response) to its upper limit: the information gained at the receptor-ligand binding step. We find that the model originally applied to cAMP sensing fails as demonstrated by the violation of the data processing inequality, i.e. the total information exceeds the information at the receptor-ligand binding step. We propose an extended model with multiple known receptor types and with cells allowed to perform several independent measurements of receptor occupancy. This does not violate the data processing inequality and implies the receptor-ligand binding noise dominates both for low and high chemoattractant concentrations. We also speculate that the interplay between exploration and exploitation is employed as a strategy for accurate sensing of otherwise unmeasureable levels of a chemoattractant.

1 Introduction

Eukaryotic amoebae *Dictyostelium discoideum* (referred as *Dictyostelium*) in vegetative state forage on bacteria by following gradients of folic acid, a by-product of bacterial metabolism [1, 2]. It is currently believed that *Dictyostelium* measure chemical gradients directly by monitoring the distribution of the occupied chemoattractant receptors. These cells can detect concentration differences as low as a few percent across their cell bodies [3, 4, 5, 6, 7, 8] and it is currently an open question what exactly limits

this process. Previously, the receptor-ligand binding fluctuations were suggested as the limiting factor, which remains a possibility since a single excited receptor may amplify the signal by activating multiple G-proteins [9, 10, 11].

Chemotaxis signaling system can be described as the following Shannon communication channel [12, 13]: the chemoattractant gradient direction as the input, the spatial distribution of occupied receptors as the intermediate step and the direction of cell motion as the output. Fuller et al. [4] recently exploited this information-theoretic framework, where a cell in a static gradient was modelled as N receptors arranged in a circle, each in chemical equilibrium with the local chemoattractant concentration, described by a dissociation constant K_d.

The joint state of all receptors θ_{rec} was assumed to depend only on the gradient direction, θ_{grad}. Likewise, the probability of cell moving in a direction θ_{res} was assumed to depend only on θ_{rec}, with these three variables forming a Markov chain: $\Theta_{grad} \rightarrow \Theta_{rec} \rightarrow \Theta_{res}$ (see SI). Capital letters denote random variables and lowercase their values. Fuller et al. [4] computed the mutual information between the gradient direction and the receptor distribution $I_{ext}(\Theta_{grad}, \Theta_{rec})$, "external mutual information". I_{ext} quantifies the information gained about the gradient through a perfect (noiseless) readout of the occupied receptors.

Furthermore, Fuller et al. [4] used *Dictyostelium* cAMP chemotaxis experiments to calculate the mutual information between the gradient direc-

tion and the cell response $I_{tot}(\Theta_{grad}, \Theta_{res})$, "total mutual information". I_{tot} quantifies the information gained about the gradient by cells through the imperfect (noisy) readout of the occupied receptors. The data processing inequality [14] (p.34) states that in a Markov chain of variables, the information can only be destroyed in each subsequent step, which here translates into $I_{tot} \leq I_{ext}$. In other words, the information gained by cells after being processed through the entire signaling pathway, cannot exceed the information gained at the receptor level. The authors [4] then argued that for low cAMP concentrations the receptor-ligand binding fluctuations dominate the entire noise ($I_{tot} \approx I_{ext}$), since there is no further information loss downstream. Previously, Ueda and Shibata [11] also reached this conclusion using signal-to-noise ratio arguments, using stochastic receptor noise and time integration with second messengers and locomotion systems.

Here, we measure the response of a population of *Dictyostelium* cells to static linear FA gradients, established in an agarose-gel based microfluidic device [15]. The steady state gradients were achieved by maintaining fixed concentrations of FA on opposite sides of a microfluidic channel (see SI). A linear gradient was established by diffusion through agarose gel. Cell migration was recorded using time-lapse optical microscopy. The measured distribution of cell displacement angles $p(\theta_{res}|\theta_{grad})$ was used to calculate the total mutual information I_{tot} and compared to I_{ext} (using the result in [4]) to test the possibility of receptor-ligand binding fluctuations dominating the total noise.

2 Results and Discussion

First, we employ the result in Fuller et al.([4], Eq.S56) for the external mutual information I_{ext} for shallow linear gradients:

$$I_{ext}(\Theta_{grad}, \Theta_{rec}) = \frac{N}{4 \ln 2 \, c(x)} \left(\frac{\nabla c}{1 + c(x)} \right)^2 \tag{1}$$

where $c(x)$ is the concentration measured in units of K_d, ∇c is the gradient measured in units of K_d/R (R is the radius of a hemispherical cell, taken as 5μm) and the dimensionless small parameter $\epsilon \equiv \nabla c/(1+c) \ll 1$. For larger values of ϵ one has to resort to numerical simulations. The design of our microfluidic device ensured it was applicable to use the Eq.1 as the small parameter was in range $0.0003 \leq \epsilon \leq 0.0065$.

Previously, Wurster and Butz [16] and de Wit and van Haastert [17] measured the dissociation constants K_d and receptor numbers N using radioligand assays. In the former case [16], we used the measured N and K_d after 3 hours in the buffer, which reflects the conditions in our experiments. In the latter case [17] vegetative cells were employed. Wurster and Butz [16] found $K_d = 150\,\mathrm{nM}$, $N = 60,000$ and de Wit and van Haastert [17] found five receptor types with the following dissociation constants and receptor numbers: 1) $K_{d1} = 450\,\mathrm{nM}$, $N_1 = 80,000$, 2) $K_{d2} = 70\,\mathrm{nM}$, $N_2 = 80,000$, 3) $K_{d3} = 17\,\mathrm{nM}$, $N_3 = 550$, 4) $K_{d4} = 50\,\mathrm{nM}$, $N_4 = 50$ and 5) $K_{d5} = 15\,\mathrm{nM}$, $N_5 = 1,450$. In both cases Scatchard plots show that the first-order kinetics can be employed with good approximation but that there is slight curvature implying either negative cooperativity or greater receptor heterogene-

ity. Furthermore, the binding curves for folic acid were taken up to μM concentrations, the interesting range explored in this study.

Second, we measured the cell trajectories and the distribution of angles $p(\theta_{res}|\theta_{grad})$ of total displacement vectors (Fig.1a) of a population of *Dictyostelium* cells (see SI for Methods). In each experiment the FA gradient was uniform and the concentration varied at most threefold across the width of a channel. Each experiment was repeated until we obtained 300 to 700 cell trajectories. These observations were used to calculate the total mutual information I_{tot} and the chemotactic index (CI). CI is defined as $\mathrm{CI} \equiv (\sum_i \overrightarrow{r_i}) \cdot \hat{n} / \sum_i |\overrightarrow{r_i}|$, where $\overrightarrow{r_i}$ is the instantaneous cell displacement during the time step i (taken as 30 seconds) and $\hat{n}$ is the gradient direction.

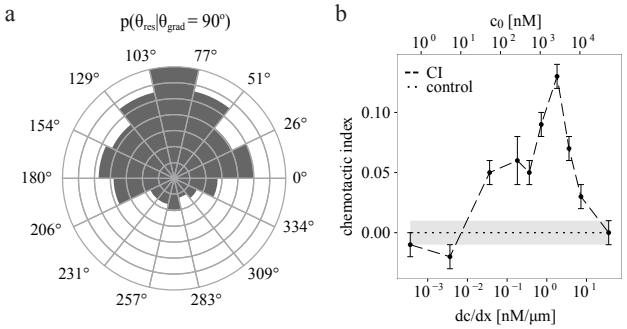

Figure 1: Measured chemotaxis response for a range of gradients and mean concentrations. (a) Distribution of cell displacement angles for the peak response for the gradient $dc/dx = 1.6\,\mathrm{nM}/\mu\mathrm{m}$ and mean concentration $c_0 = 2,500\,\mathrm{nM}$. Each radial step represents 15 data points. (b) CI for experiments with variable FA concentration in the top channel, which changed both the mean concentration and the gradient. The controls denote CI for experiments performed with no gradient with mean FA concentrations of 0 2,500 nM and 10,000 nM. The error bars and gray area denote Standard Error of the Mean (SEM).

We performed ten experiments where we varied the FA concentration in the top channel of microfluidic device while keeping the bottom channel

at concentration zero. In these experiments both the concentration and the gradient were changed and these are plotted in Fig.2a. We also performed five additional experiments (shown in Fig.2c and 2d) where we changed the mean concentration and the gradient separately. For the range of concentrations and gradients explored here, decreasing the gradient and increasing FA concentration diminished the signal. Therefore, the FA chemotaxis can depend both on the absolute value of FA concentration and its gradient.

I_{tot} was calculated by segmenting the real interval $0 \leq \theta_{res} < 2\pi$ into m bins of equal width. The bin size was $m = 14$ for all experiments, because I_{tot} with that bin size correlated extremely well with CI (compare Fig.1b and Fig.2a) for which no binning was used (see SI for further analysis). The fraction of total displacement angles n_j ending up in the bin $\theta_{res,j} \leq \theta < \theta_{res,j+1}$ was counted and I_{tot} was computed [14] (pp.247-248) as:

$$I_{tot}(\Theta_{grad}, \Theta_{res}) = \sum_{j=1}^{m} n_j \log n_j + \log m \tag{2}$$

with the error due to finite number of data points estimated as $(m-1)/2M$ [18], where M is the total number of data points.

Next, we compare I_{tot} and I_{ext}. Fig.2a shows that for low concentrations and shallow gradients $I_{tot} \approx I_{ext}$, meaning the receptor-ligand binding fluctuations dominate the total noise. This possibility was previously suggested for cAMP [7, 11] using signal-to-noise ratio analysis with a biased random walk model of cell motion. The information-theoretic analysis assumes only the steady-state receptor-ligand binding fluctuations and benefits from not

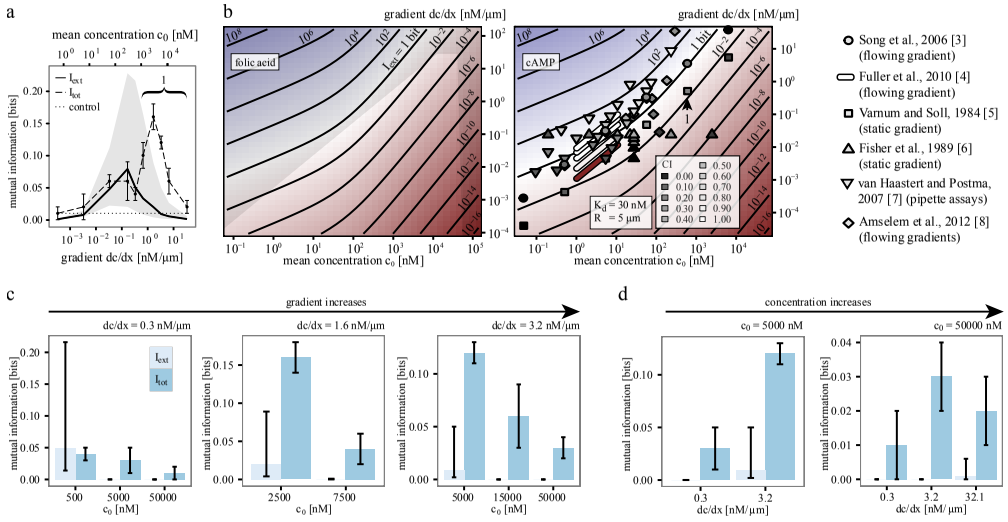

Figure 2: Comparison of the total mutual information I_{tot} and external mutual information I_{ext}. (a) I_{tot} (dashed line) and I_{ext} (solid line) for the same experiments as in Fig.1a, both averaged over all local concentrations (see SI). Error bars for I_{tot} represent SEM. The shaded range for I_{ext} denotes its spread due to the range of local concentrations the cells were exposed to in the microfluidic device (see text). Dotted line denotes the I_{tot} for control experiments without a gradient. Annotation 1 shows the range where the data processing inequality is strongly violated, $I_{tot} > I_{ext}$. (b) Left: calculated values for I_{ext} (Eq.1); shaded area denotes the combinations of c_0 and dc/dx inaccessible in our experiment due to the geometry of the microfluidic device and low solubility of FA in DB ($\sim$ 0.1 mM). Right: the range of concentrations and gradients where cAMP chemotaxis has been measured, colored by the value of measured chemotactic index, CI. The measurement with annotation 1 ($c_0 = 500$ nM $= 17$ K_d, $dc/dx = 0.5$ nM/μm $= 0.08$ K_d/R, CI=0.25) is done in approximate range where we detected the greatest violation of the data processing inequality ($c_0 = 5,000$ nM $= 33$ K_d, $dc/dx = 3.2$ nM/μm $= 0.11$ K_d/R, CI=0.13, $I_{tot} = 0.16$ bits) if we compare them by rescaling the concentrations with their respective K_ds ($K_d(\text{cAMP}) = 30$ nM, $K_d(\text{folic acid}) = 150$ nM [20, 16]). I_{tot} and I_{ext} for experiments with fixed gradient, where mean concentration is changed is shown in (c) and experiments with fixed mean concentration where the gradient is changed are shown in (d). In the range investigated here, increasing the concentration and reducing the gradient reduced the chemotaxis response, I_{tot} but the violation of the data processing inequality persists.

being tied to a particular model of cell motion, since *Dictyostelium* cells do not follow a simple random walk [19].

The most surprising result is that the response is observed for gradients as low as 0.2% across the cell body ($dc/dx = 3.2\ \mathrm{nM}/\mu\mathrm{m}$, $c_0 = 15,000\ \mathrm{nM}$, $I_{tot} = 0.06\ \mathrm{bits}$ shown in Fig.2b). For these experiments, the difference in the fraction of occupied receptors front-to-back on the cell body is given by:

$$\eta = \frac{c_{front}}{c_{front} + K_d} - \frac{c_{back}}{c_{back} + K_d} \tag{3}$$

and is shown in Table 1 for different measured dissociation constants. This fraction is at most 0.006% which amounts to a 1-10 receptors difference with 29,700 receptors (or 99%) occupied on each side, indicating a highly saturated regime. Furthermore, in this range the data processing inequality ($I_{tot} \leq I_{ext}$) is strongly violated as we have $I_{tot} > I_{ext}$. The observed response is better than theoretically possible with receptor-ligand binding fluctuations as the only noise source. Next, we compared our results with previous cAMP chemotaxis experiments [3, 4, 5, 6, 7, 8], shown in Fig.2b. In comparing critical parameters, the receptor-ligand binding constant $K_d(\mathrm{FA}) = 150\ \mathrm{nM}$ stands out as a factor of five greater compared to cAMP, $K_d(\mathrm{cAMP}) = 30\ \mathrm{nM}$, whereas the number of receptors per cell is almost the same: 60,000 for FA and 70,000 for cAMP [16, 20].

These simplified descriptions of FA and cAMP receptors were sufficient to explain the results in [4], but do not suffice here – possibly explained by the limited range of cAMP concentrations and gradients investigated in [4]

K_d nM	450	150	70	50	17	15
η	0.006 %	0.002 %	0.001 %	0.0007 %	0.0002 %	0.0002 %

Table 1: Fraction of occupied receptors front to back of the cell for the shallowest gradient where we measured the chemotaxis response, calculated using each measured receptor type according to Eq.3.

(see Fig.2b). The measurement with annotation 1 on Fig.2b from Varnum and Soll [5] supports this possibility. They measured CI=0.25 for cAMP, compared to our CI=0.13 for FA, for roughly the same mean concentration c_0 and gradient dc/dx. Therefore, the cAMP response in that range might also result in the violation of the data processing inequality. Motivated by the failure of the theory, we investigated five different modifications of the original model.

2.1 Effects of folic acid deaminase

First, we considered reduced FA concentrations perceived by cells as a result of FA deaminase activity, a protein that degrades FA [21]. We concluded, using both calculation and a series of control experiments (see SI), that it does not significantly contribute to the observed result.

2.2 Effects of multiple receptor types and receptor phosphorylation

Second, we considered all different receptor types mentioned previously. This possibility was motivated by the local minimum in I_{tot} shown in Fig.2a indicating that perhaps there are two receptor types or states, each active in a distinct ramge of local ligand concentrations. We calculated I_{ext} for each receptor type and added it together to investigate whether this resolves the violation of the data processing inequality. The results are shown in Fig.3a and indicate that the presence of multiple receptor types reduces, but does not eliminate the violation of the data processing inequality. This is because the shaded range for I_{ext} in Fig.3 represents the range of concentrations the cells were exposed to in our microfluidic device (and not the uncertainty), with the maximum value of I_{ext} corresponding to the bottom of our device and the minimum value corresponds to the top of our device. However, the systematic uncertainty of the average I_{ext} (solid line in Fig.3a) is only 10% (see SI), which is what is compared to the average I_{tot} [22]. Furthermore, the double-peak feature observed in I_{tot} is not exactly reproduced in I_{ext} even when considering only two receptor types. This could be due to the fact that I_{ext} is only an upper limit for I_{tot} and in this range the intracellular signal processing is not negligible, so $I_{tot} \ll I_{ext}$. In other words the dip could be the consequence of the extra noise somewhere downstream of the receptor-ligand binding events. It is also worth mentioning that this double-peak

response prevents us from using any single receptor with fixed K_d to fix the violation of the data processing inequality, unless the receptor number per cell N is set to a factor 12 more than it is measured.

Therefore, this explanation could be plausible only if all the cells were concentrated near the bottom of our device. In our experiments they were always uniformly distributed with the mean position in the center.

Third, we hypothesized that FA receptors can be phosphorylated. Xiao et al. [23] have shown that the phosphorylation of cAMP receptors cAR1 reduced the affinity (increased K_d) of a cAMP-cAR1 process by a factor of three, from 300 nM to 900 nM. Here we assume that the additional receptor types can be phosphorylated to $3 \times K_d$ and fit the data in the same way as for additional receptor types. The results (Fig.3b) show that this only reduced the violation of the data processing inequality, but did not eliminate it.

2.3 Effects of cell polarization

Fourth, we considered for the possibility of cell polarization [24], previously considered in [13, 25]. In our analysis thus far, we assumed that cells had no previous knowledge of the gradient direction, so the prior probability was $p(\theta_{grad}) = 1/2\pi$. Now, we consider a circular normal prior distribution:

$$p(\theta_{grad}) = \frac{\exp(K \cos \theta_{grad})}{2\pi I_0(K)} \tag{4}$$

where $I_0(K)$ is the modified Bessel function of the first kind of zeroth order, and the parameter K measures the bias strength. We used the approach

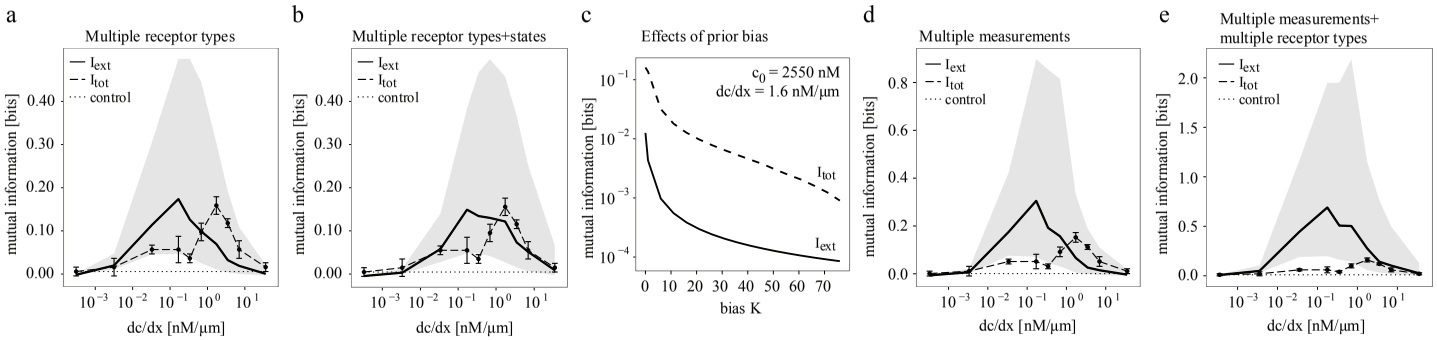

Figure 3: I_{tot} and I_{ext} for models with additional assumptions. (a) Fit of our data to the model with multiple receptor types; see text for details. (b) Fit of our data to the model with multiple receptor types and the hypothesis that they can be phosphorylated to states with three-fold higher $K_d = 1,350\,\mathrm{nM}$. (c) Calculation for biased I_{tot} and I_{ext}, where the uniform prior distribution was replaced with a circular normal distribution. Both I_{tot} and I_{ext} are plotted as a function of bias parameter K (large K values correspond to very sharp prior distributions), showing that the violation of data processing inequality persists even for biased cells. (d) Comparison of I_{tot} and I_{ext} for a model with multiple independent measurements of receptor occupancy which still results in the violation of the data processing inequality. (e) Model with combined effects of (a) and (d) does not result in the violation of the data processing inequality and successfully explains the data.

from [25] to numerically calculate $I_{ext}^{bias}(K)$. We also numerically calculated $I_{tot}^{bias}(K)$ (see SI) and then compared both I_{tot}^{bias} and I_{ext}^{bias} up to very biased distributions with $K = 80$, as larger values required significantly higher numerical precision. Fig.3c shows that the violation of the data processing inequality still persists.

2.4 Effects of multiple measurements

Finally we investigated the effect of multiple independent measurements of the receptor occupancy [7, 11], occuring if cells can choose between i) short and imprecise gradient measurements, but moving fast and ii) long and precise gradient measurements but moving more slowly. This is known as the tradeoff between exploration and exploitation in the field of reinforcement learning [26].

Eq.1 is only valid for a single snapshot measurement. The information acquired from multiple independent measurements is simply the sum of the information of each contribution due to a single measurement. Therefore we multiply the Eq.1 by the number of independent measurements $N_{meas} = T_{pseudo}/T_{correl}$ [4, 25], where T_{pseudo} is the time scale of pseudopod extension and T_{correl} is the receptor correlation time (this ratio gives us the maximum number of measurements that could have been performed). We note that T_{pseudo} is likely the upper bound for the integration time based on the evidence in variable gradient experiments [27] where it was observed

that the cells extend their pseudopods in the gradient direction as soon as the direction of the gradient is changed. Rappel and Levine previously noted that the correlation time consists of both receptor chemical dynamics and the diffusive process and estimated the cAMP receptor correlation time $T_{correl} = 5\mathrm{s}$ [28, 29]. Fuller et al.[4] concluded $N_{meas}^{cAMP} \approx 1$. We estimated N_{meas}^{FA} by assuming that T_{pseudo} is inversely proportional to the mean cell speed, and the same T_{correl} for both FA and cAMP receptors (based on comparable receptor off-rates for FA and cAMP receptors [17, 30]):

$$N_{meas}^{FA} = \frac{T_{pseudo}^{FA}}{T_{correl}} \approx N_{meas}^{cAMP} \frac{v_{cAMP}}{v_{FA}} \tag{5}$$

where the chemotaxis speeds are: $v_{cAMP} = 0.25\mu\mathrm{m/s}$ [4] and $0.05\,\mu\mathrm{m/s} \leq v_{FA} \leq 0.12\,\mu\mathrm{m/s}$, which gives $2 \leq N_{meas}^{FA} \leq 4$. I_{tot} and I_{ext} are compared in Fig.3d and show that this only reduced the violation of the data processing inequality, but again does not eliminate it. Recently developed approaches considered diffusible inhibitors in balanced inactivation model [31, 28, 29] and their integration time ($T_{int} = 10$ s) corresponds roughly to the integration times estimated here ($T_{int} = 10$ to 20 s). In addition, the models considered so far do not reproduce the double peak observed experimentally (Fig.3), but this might be the consequence of a significant information loss downstream of the receptor-ligand binding events.

However, combining the effects of additional receptor types and multiple independent measurements does not result in the violation of the data

processing inequality; see Fig.3e. N_{meas}^{FA} roughly agrees with [7] $N_{meas}^{cAMP} \approx 2$, which was included to explain a much greater range of concentrations and gradients than in [4] (see Fig.2b).

It should still be noted that the multiple independent measurements can be a consequence of integrating the information from multiple pseuodopods [24]. During the 30 second time interval cells extend a number of small protrusions (sometimes simultaneously), some of which are retracted quickly (see Fig.6 in [32]). Taking this into account would lead to a different definition of the total mutual information than that used here where the centroid of each cell is used to specify its position. One direction for future studies is then to perform experiments with higher resolution to quantify the information acquired about the gradient, employing this alternative measure.

2.5 Other effects

Fig.3e implies that the total noise is indeed dominated by the receptor-ligand binding fluctuations at both low and high gradients and concentrations. This seems plausible since in that range the receptors are either mostly unoccupied or occupied. In the intermediate range where $I_{ext} \gg I_{tot}$, the internal noise dominates. We note that it has been shown [33] that there is always a fraction of cell population which does not respond to gradients and polarizes in random directions, independent of the external cAMP gradient. Since in our experiments we only have static gradients we could

not separately identify these cells and they had to be included in the data analysis. Exclusion of this subpopulation from our analysis would increase the total mutual information I_{tot} even further and the violation of the data processing inequality would be even larger.

The possibility of receptor interactions was ruled out due to uniform receptor distributions for both FA [34] and cAMP receptors [35, 36]. Unlike in the cAMP case [4], here the non-circularity of cell shapes is not an issue since the cells are circular when sensing FA. However, there is still a possibility of a more complicated mechanism if FA receptors also transport FA into the cell [9], serving as a different communication channel, or if a FA transporter is a separate protein, as a separate communication channel.

The possibility that FA and cAMP receptors share the majority of the internal signaling pathway [37] implies equal FA and cAMP responses, if rescaled by their respective parameters K_d and N. This remains to be investigated with more cAMP and FA chemotaxis measurements in the same concentration and gradient range. The results here and in [4, 11] confirmed that the external noise dominates for both chemoattractants in low concentration range. This is in contrast with the conclusion in [33],SI possibly caused by using single-pulse temporal gradients, as opposed to defined static gradients used here and in [4].

Acknowledgments

We thank Petra Fey (Dicty Stock Center, Northwestern University) for AX4 cell lines, advice and suggestions about media preparation, Richard Kessin (Columbia University), Jeffrey Hadwiger (Oklahoma State University), David Knecht (University of Connecticut) for valuable advice regarding the choice and preparation of chemotacting media and helpful suggestions, Elijah Bogart (Cornell University) for contributions to the microfluidic device design and strategic planning, Mingming Wu (Cornell University), Kevin Tharratt (Cornell University) for fruitful discussions, Kees Weijer (University of Dundee) Ariana Strandburg-Peshkin (Princeton University), Eric Siggia (Rockefeller University/Cornell University) and Nives Skunca (ETH Zurich) for useful comments, Herbert Levine and Wouter-Jan Rappel (University of California, San Diego) for helpful advice, Eberhard Bodenschatz (Max Planck Institute Goettingen, Germany/Cornell University) for generous advice and equipment, anonymous referees for helpful and insightful suggestions and ACCEL Cornell Engineering Lab for use of the COMSOL Multiphysics software.

This work was supported by National Institutes of Health grant (P01 GM078586).

References

[1] Kessin RH. 2001 *Dictyostelium: evolution, cell biology, and the development of multicellularity*, Cambridge: Cambridge University Press.

[2] Pan P, Hall EM & Bonner JT. 1972 Folic Acid as Second Chemotactic Substance in the Cellular Slime Moulds. *Nat. New Biol.* 237, 181-182.

[3] Song L, Nadkarni SM, Bodeker HU, Beta C, Bae A, Franck C, Rappel W-J, Loomis WF & Bodenschatz E. 2006 Dictyostelium discoideum chemotaxis: Threshold for directed motion. *Eur. J. Cell Biol.* 85, 981-989.

[4] Fuller D, Chen W, Adler M, Groisman A, Levine H, Rappel W-J & Loomis WF. 2010 External and internal constraints on eukaryotic chemotaxis. *Proc. Natl. Acad. Sci. USA* 107, 9656-9659.

[5] Varnum B & Soll DR. 1948 Effects of cAMP on Single Cell Motility in Dictyostelium. *J. Cell Biol.* 99, 1151-1155.

[6] Fisher PR, Merkl R & Gerisch G. 1989 Quantitative Analysis of Cell Motility and Chemotaxis in Dictyostelium discoideum By Using an Image Processing System and a Novel Chemotaxis Chamber Providing Stationary Chemical Gradients. *J. Cell Biol.* 108, 973-984.

[7] van Haastert PJM & Postma M. 2007 Biased Random Walk by Stochastic Fluctuations of Chemoattractant-Receptor Interactions at the Lower Limit of Detection. *Biophys. J.* 93, 1787-1796.

[8] Amselem G, Theves M, Bae A, Beta C & Bodenschatz E. 2012 Control Parameter Description of Eukaryotic Chemotaxis. *Phys. Rev. Lett.* 109, 108103.

[9] Lauffenburger DA & Linderman JJ. 1993 *Receptors: Models for Binding, Trafficking and Signaling.*, Oxford University Press, pp 335.

[10] Devreotes PN & Zigmond SH. 1988 Chemotaxis in Eukaryotic Cells: a focus on leukocytes and Dictyostelium. *Annu. Rev. Cell. Biol.* 4, 649-686.

[11] Ueda M & Shibata T. 2007 Stochastic Signal Processing and Transduction in Chemotactic Response of Eukaryotic Cells. *Biophys. J.* 93, 11-20.

[12] Shannon CE. 1948 A Mathematical Theory of Communication. *Bell System Technical Journal* 27, 379-423 & 623-656.

[13] Andrews BW & Iglesias PA. 2007 An information-theoretic characterization of the optimal gradient sensing response of cells. *PLoS Comput. Biol.* 3(8):e153.

[14] Cover TM & Thomas JA. 2005 *Elements of Information Theory*, 2nd Ed., New York: Wiley, pp 34-35.

[15] Cheng SY, Heilman S, Wasserman M, Archer S, Shulerac ML & Wu M. 2007 A hydrogel-based microfluidic device for the studies of directed cell migration. *Lab Chip.* 7, 763-769.

[16] Wurster B & Butz U. 1980 Reversible Binding of the Chemoattractant Folic Acid to Cells of Dictyostelium discoideum. *Eur. J. Biochem.* 109, 613-618.

[17] De Wit RJW & van Haastert PJM. 1985 Binding of folates to Dictyostelium discoideum cells. Demonstration of five classes of binding sites and their interconversion. *Biochim. Biophys. Acta.* 814, 199-213.

[18] Roulston MS. 1999 Estimating the errors on measured entropy and mutual information. *Physica D* 125, 285-294.

[19] Li L, Norrelykke SF & Cox EC. 2008 Persistent Cell Motion in the Absence of External Signals: A Search Strategy for Eukaryotic Cells. *PLoS ONE* 3(5):e2093.

[20] van Haastert PJM. 1983 Binding of cAMP and adenosine derivatives to Dictyostelium discoideum cells. *J. Biol. Chem.* 258, 9643-9648.

[21] Kakebeeke PIJ, De Wit RJW & Konijn TM. 1980 Folic Acid Deaminase Activity During Development in Dictyostelium discoideum. *J. Bacteriol.* 143, 307-312.

[22] We appreciate the comments of anonymous referees and Eric Siggia on this matter.

[23] Xiao Z, Yao Y, Long Y & Devreotes P. 1999 Desensitization of G-protein-coupled receptors: agonist-induced phosphorylation of the chemoat-

tractant receptor cAR1 lowers its intrinsic affinity for cAMP. *J. Biol. Chem.* 274, 1440-1448.

[24] We thank an anonymous referee for this suggestion.

[25] Hu B, Chen W, Levine H & Rappel WJ. 2011 Quantifying information transmission in eukaryotic gradient sensing and chemotactic response. *J. Stat. Phys.* 142, 1167-1186.

[26] Sutton RS & Barto AG1998. *Reinforcement Learning: An Introduction (Adaptive Computation and Machine Learning)* Cambridge, MA: MIT Press.

[27] Srinivasan K, Wright GA, Hames N, Housman M, Roberts A, Aufderheide KJ & Janetopoulos C. 2013 *J. Cell Sci.* 126, 221-33. doi: 10.1242/jcs.113415

[28] Rappel WJ & Levine H. 2008 Receptor noise and directional sensing in eukaryotic chemotaxis. *Phys. Rev. Lett.* 100, 228101.

[29] Rappel WJ & Levine H. 2008 Receptor noise limitations on chemotactic sensing. *Proc. Natl. Acad. Sci USA* 105, 19270-19275.

[30] Ueda M, Sako Y, Tanaka T, Devreotes P & Yanagida T. 2001 Single-molecule analysis of chemotactic signaling in Dictyostelium cells. *Science* 294, 864:867.

[31] Levine H, Kessler DA & Rappel WJ. 2006 Directional sensing in eukaryotic chemotaxis: A balanced inactivation model. *Proc. Natl. Acad. Sci. USA* 103, 9761-9766.

[32] Xiong Y, Kabacoff C, Franca-Koh J, Devreotes PN, Robinson DN & Iglesias PA. 2010 Automated characterization of cell shape changes during amoeboid motility by skeletonization. *BMC Syst. Biol.* 4:33 doi:10.1186/1752-0509-4-33

[33] Samadani A, Mettetal J & van Oudenaarden A. 2006 Cellular asymmetry and individuality in directional sensing. *Proc. Natl. Acad. Sci. USA* 103, 1549-1554.

[34] Rifkin JL. 2001 Folate Reception by Vegetative Dictyostelium discoideum Amoebae: Distribution of Receptors and Trafficking of Ligand. *Cell Motil. Cytoskeleton* 48, 121-129.

[35] Xiao Z, Zhang N, Murphy DB & Devreotes PN. 1997 Dynamic distribution of chemoattractant receptors in living cells during chemotaxis and persistent stimulation. *J. Cell. Biol.* 139, 365-374.

[36] Skoge M. 2009 PhD thesis.

[37] King JS & Insall RH. 2009 Chemotaxis: finding the way forward with Dictyostelium. *Trends Cell Biol.* 19, 523-530.

High fidelity information processing in folic acid chemotaxis of Dictyostelium amoebae: Supplementary Information

Igor Segota, Surin Mong, Eitan Neidich, Archana Rachakonda, Catherine J. Lussenhop and Carl Franck

1 Methods

1.1 Information measures

Shannon's information theory frees the data analysis from being tied to any particular model (as an example of successful applications see e.g. [1] and [2]) – and in this case, from any particular details of signal transduction pathways, but still provides quantifiable relationships between inputs and outputs. The relevant quantities in information theory are defined as follows [3]. The information entropy of a random variable X, is measured in bits defined as $H(X) = -\int p(x) \log_2 p(x) dx$ (a definite integral defined over the entire range where X is defined). It is a measure of "sharpness" of probability distribution $p(x)$; a perfectly sharp probability distribu-

tion has entropy zero, whereas a perfectly flat, uniform distribution gives the highest possible value for entropy $H(X)$. An alternative interpretation of information entropy is the number of bits or the amount of information required to describe the random variable X. Sharp probability distributions require fewer bits for their full description than flat probability distributions. Intuitively, for the former only a few values near the peak can be sufficient to describe most of the outcomes of X, while for the latter we need more information to achieve the same. For conditional probability distributions, the conditional entropy is measured in bits defined as $H(X|Y) = -\int dyp(y) \int dxp(x|y) \log_2 p(x|y)$. This measures how sharp $p(x|y)$ is, when averaged over all possible values of y. For some values y, $p(x|y)$ may be sharp, for some other values of y, $p(x|y)$ may not be so sharp, and the conditional entropy tells us on average what is the sharpness, when averaged over all possible y. The average *gain* in information about x, given y, is the difference between the two, called mutual information $I(X,Y) = H(X) - H(X|Y)$. This measure describes the increase in knowledge about X after we have been given some value y, and then averaged over all possible y. In other words, $I(X,Y)$ describes how much on average $p(x|y)$ is sharper, when compared to $p(x)$. The sharper the probability distribution becomes, the more information we have acquired about a random variable X.

1.2 Application to gradient sensing

In this case, the sensing process essential to eukaryotic chemotaxis is depicted in Fig. 1a. Here we consider three random but conditionally dependent variables, the gradient direction θ_{grad}, the receptor occupancy θ_{rec} and the cell response directions θ_{res}. These variables are assumed to form a Markov chain (see Fig.1b), where the cell response is conditionally dependent on the distribution of occupied receptors; i.e. given the distribution of occupied receptors, the cell response is completely independent of the original direction of the gradient that caused this particular receptor occupancy. Due to noise, the same receptor occupancy distribution can occur for gradients pointing in different directions. Without any prior knowledge we assume the gradient is equally likely to be pointing in any direction. We will see how much information we can obtain about the gradient by either observing the cell response and by calculating the distribution of receptor occupancy, and then comparing the two gains. The mutual information $I_{tot}(\theta_{grad}, \theta_{res}) = H(\theta_{grad}) - H(\theta_{grad}|\theta_{res})$ quantifies the total amount of information cells gained about the gradient (or by how much the entropy of θ_{grad} is reduced); this is determined by observing their response (see Fig.1c). Therefore, I_{tot} is the gain in information that includes all possible noise sources in the FA signal transduction pathway.

In addition, the (external) mutual information (see Fig.1c) between the

gradient direction and receptor occupancy

$$I_{ext}(\theta_{grad}, \theta_{rec}) = H(\theta_{grad}) - H(\theta_{grad}|\theta_{rec}) \quad (1)$$

tells us the information gained about the gradient by knowing the distribution of receptors occupied with FA. Authors in [4] formulated a theory for computing this quantity and gave an analytical result applicable for shallow gradients. The assumptions behind this theory are: i) the steady state of the receptor-ligand binding process, ii) the first part of the Markov chain model shown in Fig.1b (receptor probability distribution is affected only by the local gradient), iii) cells of perfectly circular shapes and iv) uniform receptor distribution. While we have no direct way of confirming the plausible assumptions i) and ii) when sensing FA, *Dictyostelium* do have circular shapes and the distribution of FA receptors was previously measured as uniform [5]. This theory gives predictions for the external mutual information I_{ext} using only two biochemical constants – the dissociation constant K_d between FA and its receptor and the total receptor number per cell, N. Both have been measured previously and multiple receptor types/states have been discovered as is also the case for cAMP receptors (see main text for discussion). The dissociation constant and the total receptor number per cell, as well as the experimentally fixed FA concentration and its gradient in our devices are sufficient to predict the external mutual information I_{ext}. I_{ext} provides the upper limit for the amount of information that can be acquired (I_{tot}), due to the data processing inequality: $I_{tot} \leq I_{ext}$ [7]. In other

words, any kind of data processing can only destroy information. If the two quantities are roughly similar $I_{tot} \approx I_{ext}$, then the gain in information about θ_{grad} is about the same for both cases and the majority of the noise in the entire process comes from receptor-ligand binding events.

1.3 Cell growth and preparation

Cells of the well characterized axenic strain, AX4 (provided by Dictyostelium Stock Center, Northwestern University), were grown in shaken culture suspension at 150 RPM in Formedium HL5 (Formedium, Hunstanton, UK) with glucose culture medium up to the concentration of about $0.5 - 3 \times 10^6$ cells. Development Buffer (DB; DictyBase recipe: 5 mM Na_2HPO_4, 5 mM KH_2PO_4, 1 mM $CaCl_2$, 2 mM $MgCl_2$; pH 6.5) was chosen as the medium for FA chemotaxis experiments because it is a well-defined medium and is an approximation of a physiological environment due to its low ionic strength [8]. A negative aspect of using DB is cell starvation and progression into development after 6+ hours (depending on cell density) and eventual loss of FA chemotactic sensitivity [9]. This was circumvented by performing the experiment before the starvation response occurs, as indicated by cell morphology – cells still had circular shapes. Since it was shown that the HL5 medium already contains about 0.12 mg/l of FA [10] ($\sim$0.3 μM), the medium was diluted by factor 30,000$\times$, lowering the background FA concentration in the medium to at most 0.01 nM. This corresponds to about

1 molecule of FA per volume size of a Dictyostelium cell ($100\,\mu\mathrm{m}^3$). Depending on the cell concentration, 1-5 ml of cell suspension was taken from the shaken culture and DB was added for a total volume of 10 ml (dilution $\geq 2\times$). The cell suspension was then centrifuged for 40 seconds at 1000 RPM (200 g force), 9.8 ml of supernatant was removed, and 9.8 ml of DB was added to again have the final volume of 10 ml (dilution $50\times$); this was repeated once more (another dilution of $50\times$). 9.8 ml of supernatant was removed again and finally, 0.2 ml of $1\mu\mathrm{m}$ diameter colloidal particles at concentration 10^8 particles/ml (Polysciences, Inc.) in DB and 1-5 ml of DB was added, depending on the starting cell concentration (dilution $6\times$). The colloidal particles allowed us to monitor unintended convection that could ruin the static gradient. The entire procedure took about 20-30 minutes after which the cells were immediately loaded into the microfluidic device with an already established gradient.

1.4 Microfluidics device design

The microfluidic device was designed as an agarose gel containing 3 channels [11]: the static middle channel and two flowing side channels, that represent fixed boundary conditions, were separated by a layer of agarose gel and the gradient was formed by waiting for diffusion of FA to reach a steady state (see Fig.2 and Fig.3). Reservoirs were connected via Teflon tubing and the steady flow was supplied by a Harvard PHD 2000 syringe pump. The

time to reach the steady state was checked by running a 2D diffusion simulation in COMSOL Multiphysics 3.5 (COMSOL, www.comsol.com) and analyzing the gradient in the middle of the channel (Fig.3). The microfluidic channel containing Dictyostelium cells, also contained 1μm-sized colloidal particles. These were used to monitor the flow rate in the static channel and the measured Peclet number Lv/D (dimensionless number characterizing the ratio of advective versus diffusive transport) was always below 0.3, where L is the channel height (250 μm), D the diffusion constant of folic acid 194 μm^2/s [12] and v the measured average drift velocity of colloidal particles (0.04 to 0.23 μm/s). After loading the cells, the gradient in the middle channel was temporarily lost, however, the time-scale of diffusive refilling of that channel from the bulk of the material above is estimated to be only $t \sim L^2/D \approx 5$ minutes, an insignificant duration.

1.5 Device preparation

The 3% agarose gel was formed as follows. 0.300g of agarose was mixed with 10 ml of DB. The agarose mixture was heated and kept near the boiling point in a microwave oven for 40 seconds total. Agarose was molded by pouring the heated mixture over an inverted PDMS master, which was itself molded from an original Teflon master produced by conventional milling. After about 2 minutes the agarose solidified, the holes were punched and the chamber was secured between a plexiglas manifold and a glass micro-

scope slide. In this experiment 3% agarose serves as an environment permeable to small molecules, such as water and folic acid, but not permeable to Dictyostelium. Dictyostelium are migrating naturally attached on the glass surface, with 250 μm of static liquid (DB+FA gradient) on top and around them. The agarose gel was sealed well enough that the cells were unable to crawl underneath it.

1.6 Cell recording

For each run, at t=0 hours: the gradient formation was started. At t=3 hours: the cells were loaded in the device. Since we noticed that cells were not very mobile when first introduced into the device, we allowed them to adjust to the new environment for about 3.3 hours to establish a good degree of mobility. At t=6.3 hours recording started. At t=9.3 hours: the recording stopped. This time was chosen based on the fact that this is the time when one would first observe morphological changes associated with cell-to-cell cAMP signaling during the starvation response (e.g. elongated cells and formation of streams) when the cell density was significantly (10x) higher. Cell motion was recorded using bright field time-lapse optical microscopy, using an Olympus IX71 inverted microscope and a Home Science Tools MI-DC5000 5.0 Megapixel camera. Snapshots were taken every 30 seconds and cell trajectories were later analyzed on a computer. The list of concentrations used in both channels is shown in Table I.

combination	$dc/dx\,(\mathrm{nM}/\mu\mathrm{m})$	$c_0\,(\mathrm{nM})$	$c_{\mathrm{high}}\,(\mathrm{nM})$	$c_{\mathrm{low}}\,(\mathrm{nM})$
1	3.20×10^{1}	5.0×10^{4}	1.00×10^{5}	0
2	6.4×10^{0}	1.0×10^{4}	2.00×10^{4}	0
3	3.2×10^{0}	5.0×10^{3}	1.00×10^{4}	0
4	1.6×10^{0}	2.5×10^{3}	5.00×10^{3}	0
5	6.4×10^{-1}	1.0×10^{3}	2.00×10^{3}	0
6	3.2×10^{-1}	5.0×10^{2}	1.00×10^{3}	0
7	1.6×10^{-1}	2.5×10^{2}	5.00×10^{2}	0
8	3.2×10^{-2}	5.0×10^{1}	1.00×10^{2}	0
9	3.2×10^{-3}	5.0×10^{0}	1.00×10^{1}	0
10	3.2×10^{-4}	5.0×10^{-1}	1.00×10^{0}	0
11	0	0	0	0
12	0	2.5×10^{3}	2.50×10^{3}	2.50×10^{3}
13	0	1.0×10^{4}	1.00×10^{4}	1.00×10^{4}
14	3.2×10^{-1}	5.0×10^{3}	5.50×10^{3}	4.50×10^{3}
15	1.6×10^{0}	7.5×10^{3}	1.00×10^{4}	5.00×10^{3}
16	3.2×10^{0}	1.5×10^{4}	2.00×10^{4}	1.00×10^{4}
17	3.2×10^{0}	5.0×10^{4}	5.50×10^{4}	4.50×10^{4}
18	3.2×10^{-1}	5.0×10^{4}	5.05×10^{4}	4.95×10^{4}

Table 1: List of experimentally used concentrations in the two channels of a microfluidic device, c_{high} and c_{low} with calculated gradient dc/dx and the mean concentration c_0.

1.7 Analysis of cell trajectories

We used ImageJ (http://imagej.nih.gov/ij/) with ParticleTracker Plugin [13] for automated cell detection and tracking. Particle tracks were analyzed in a custom-made MATLAB (The MathWorks, Natick, MA) code, where the following filtering was applied: the cells that could not be tracked consistently for more than 6 minutes (3% of the total recording time) were discarded and points on the screen that did not move at all were discarded as well; the latter corresponding to dead cells or other artifacts on the glass surface or CCD. Each experimental run was repeated 3 to 11 times, until about 300 to 700 cell trajectories were gathered. A sample of such trajectories is shown in Fig.4. The distribution of trajectories was very broad with lengths of $260 \pm 220 \mu\mathrm{m}$. Depending on the gradient, component of the velocity in gradient direction ranges from $-0.15\ \mu\mathrm{m/min}$ to $0.51\ \mu\mathrm{m/min}$.

1.8 Analysis of different trajectory time lengths

Here we experimentally check for the possibility that cells can integrate multiple gradient measurements over time scales longer than the pseudopod extension time ($\sim 30\ \mathrm{s}$). We calculated the chemotactic index (CI) as we progressively moved the end point of the cell trajectory from the one at frame 2 (30 seconds) to the one at frame 400 (3.3 hours).

The 30 second time interval between subsequent frames was chosen since the cell displacements were typically about $3\ \mu m$, which was at the

limit for measuring displacements in our experiments.

If the cells were indeed integrating over more measurements as the time moved on, we would expect to see the CI increase with time. The results for our peak experiments with the mean concentration of $2.5\ \mu\mathrm{M}$ and the gradient of $1.6\ \mathrm{nM}/\mu\mathrm{m}$ are shown in Fig.7. Here we see that CI actually slightly decreases after $\sim\ 300\ \mathrm{s}$, but overall does not change significantly.

2 Averaging the external mutual information

External mutual information I_{ext} was averaged over the entire channel in the gradient direction, weighted by the fraction of cells in each spatial segment:

$$\langle I_{ext}\rangle = \sum_{i=1}^{M} p_i I_{ext,i} \tag{2}$$

where p_i is the fraction of cells in a segment i of the microfluidic device (a sample of such distribution is shown in Fig.8) and $I_{ext,i} = I_{ext}(\langle c(x_i)\rangle)$ is the external mutual information for the average concentration in segment i. If I_{ext} is averaged assuming a perfectly uniform cell distribution:

$$\langle I_{ext}\rangle = \frac{1}{c_{max}-c_{min}}\int_{c_{min}}^{c_{max}} I_{ext}(c_0)dc_0 \tag{3}$$

the analytical result is:

$$\langle I_{ext}\rangle = \frac{N}{4\ln 2\,(c_{max}-c_{min})}\times \left\{\frac{1}{1+c_{max}} - \frac{1}{1+c_{min}} - \ln\left[\frac{(1+c_{min})c_{max}}{c_{min}(1+c_{max})}\right]\right\}$$

which agrees to our estimate of $\langle I_{ext}\rangle$ to about 10% for our experiments.

3 Effects of folic acid degradation

Here we explore the possibility that most of the FA is degraded by cells themselves, and they were effectively sensing a lower FA concentration, closer to K_d. FA can be degraded by an extracellular form of FA deaminase protein and we estimate the extent to which the FA concentration can be reduced by this process. Following up on the previous study of the level of deaminase secretion under the same conditions [14], we estimated the deaminase activity (defined as the amount of FA degraded per cell per unit time) for our system. The reported mean value for the deaminase activity from [14] is 35 pmol per 10^6 cells per minute. Assuming a steady-state flat concentration profile of deaminase in our experiment of total volume of 0.15 ml, about 50 cells in total and about 5 hours the cells spent in the chamber (corresponding to the middle of our run), the amount of FA that could possibly be degraded by that time is 5.25×10^{-13} mol. On the other hand, the total amount of FA in this entire volume, at $2.5\,\mu\mathrm{M}$ mean concentration is 3.75×10^{-10} mol, so the degradation by FA deaminase could account for less than 0.1% of the expected amount of FA. This calculation is summarized in the Table 2. This conclusion was verified experimentally by changing the cell density by a factor of four (from 7 cells/mm^2 to 30 cells/mm^2) for the gradient where we observed peak response and noticing that the same result in terms of chemotactic index (0.10 ± 0.02 at lower vs 0.09 ± 0.01 at higher density) and total mutual information (0.14 ± 0.02 bits vs 0.14 ± 0.01 bits)

quantity	value	units
activity	35×10^{-6}	pmol/(cell min)
total volume	0.15	ml
time	300	min
cell number	50	
FA amount	3.75×10^{-10}	mol
FA amount degraded	5.25×10^{-13}	mol
FA percentage degraded	0.07	%

Table 2: Summary of the calculation for FA deaminase contribution to the observed results for the case of our best response at $2.5\,\mu\mathrm{M}$ mean concentration.

was observed. Thus, we conclude that degradation of FA by FA deaminase cannot account for the violation of the data processing inequality.

4 Effects of cell polarization / bias

The total mutual information with bias is defined by:

$$I_{tot}^{bias} = H_{bias}(\theta_{res}) - H_{bias}(\theta_{res}|\theta_{grad}) \tag{4}$$

with

$$H_{bias}(\theta_{res}) = -\int p(\theta_{res}; K) \log_2 p(\theta_{res}; K) d\theta_{res} \tag{5}$$

$$H_{bias}(\theta_{res}|\theta_{grad}) =$$

$$-\iint p(\theta_{res}|\theta_{grad}) p(\theta_{grad}) \log_2 p(\theta_{res}|\theta_{grad}) d\theta_{grad} d\theta_{res}$$

where the marginal probability of a response at an angle θ_{res} is:

$$p(\theta_{res}; K) = \int p(\theta_{res}|\theta_{grad})p(\theta_{grad})d\theta_{grad} \tag{6}$$

which is calculated using the experimentally measured values for the distribution of the response given the gradient, $p(\theta_{res}|\theta_{grad}) = p(\theta_{res} - \theta_{grad})$. Since the measured values were discrete, we originally approximated the integral in Eq.2 (in the main text) with a discrete sum. However, here we calculated a more complicated integral and instead approximated a discrete distribution $p(\theta_{res}|\theta_{grad})$ with a continuous distribution using kernel density estimation [15]. Since this is a different method of estimating the total mutual information from the data, we first compared the results for non-biased total mutual information (corresponding to the case $K = 0$) obtained using these two methods in Fig.9 and show they are very similar. We therefore used the kernel density estimation to compute the biased total mutual information, for various values of the biasing parameter $K > 0$.

Next, we numerically calculated the biased external mutual information I_{ext}^{bias} using the Eq.13 in [16]:

$$I_{ext}^{bias} = I_{ext} - B(K) \tag{7}$$

where the term $B(K)$ depends on the bias (see [16] for details).

$$I_{ext}^{bias} = I_{ext} - \int p(\rho)h(\rho; K_p)d\rho \tag{8}$$

with:

$$I_{ext} = \frac{1}{\ln 2}\left(\frac{\nu}{\sigma}\right)^2 - \int p(\rho)\log_2 I_0\left(\frac{\rho\nu}{\sigma^2}\right)d\rho \tag{9}$$

$$p(\rho;\nu,\sigma) = \frac{\rho}{\sigma^2}\exp\left[-\frac{\rho^2+\nu^2}{2\sigma^2}\right] I_0\left[\frac{\rho\nu}{\sigma^2}\right] \tag{10}$$

$$\nu(N, c_0, \nabla c) = \frac{N}{2}\frac{\nabla c}{c_0+1} \tag{11}$$

$$\sigma(N, c_0) = \sqrt{\frac{N}{2}\frac{c_0}{(c_0+1)^2}} \tag{12}$$

$$h(\rho; K_p) = \frac{1}{\ln 2}\left[K\frac{I_1(K_p)}{I_0(K_p)} - \ln I_0\left(\frac{\rho\nu}{\sigma^2}\right)\right] \tag{13}$$

$$K_p = \frac{K\nu\rho}{K\sigma^2+\nu\rho} \tag{14}$$

where c_0 is the local chemoattractant concentration in units of K_d, ∇c the gradient in units of K_d/R, N the total number of receptors, K the same biasing parameter and $I_0(K_p)$, $I_1(K_p)$ are the modified Bessel functions of the first kind of order zero and one, respectively. We computed both the total and external mutual information for different magnitudes of the bias, up to very sharp polarizations $K = 80$ (larger values require significantly higher numerical precision) and show the results in Fig.3c in the main text. These results show that the inclusion of this effect still results in the violation of the data processing inequality, and moreover, for a wide range of bias parameters, the violation is further increased.

5 Effects of binning

The total mutual information calculated using Eq.3 (main text) depends on the choice of number of bins m.

While there is no "best" number of bins, here the total number of bins chosen was 14 which gave similar results for all combinations of gradients

and mean concentrations since we had roughly the same number of cells in each case (typically around 500). First, as stated in the main text, it correlates well with the CI (comparing Fig.1b and 2a in the main text). Second, I_{tot} reaches a plateau in this bin range and becomes lower when we use too few bins (below ≈ 10) or higher but with much larger uncertainty if we use too many bins (roughly 30 or more); see Fig.10. The plateau corresponds to the middle ground here where I_{tot} does not change much if the bin number changes a little around the chosen value. Finally, this choice of 14 bins gave approximately the same results as the Kernel Density Estimate (Fig.9) used for data smoothing [15].

References

[1] S.P. Strong, R. Koberle, R.R.D. van Steveninck, W. Bialek 1998. Phys. Rev. Lett. 80:197-200

[2] T. Gregor, D.W. Tank, E.F. Weischaus, W. Bialek 2007. Cell 130:153-164

[3] C.E. Shannon 1948. Bell Syst. Tech. J. 27:379-423 and 623-656

[4] D. Fuller, W. Chen, M. Adler, A. Groisman, H. Levine, W.-J. Rappel and W.F. Loomis 2010. Proc. Natl. Acad. Sci. USA 107:9656-9659

[5] J.L. Rifkin 2001. Cell Motil. Cytoskeleton. 48:121-129

[6] B. Wurster and U. Butz 1980. Eur. J. Biochem. 109:613-618

[7] T.M. Cover and J.A. Thomas 2005. Elements of Information Theory. Wiley, New York, 2nd Ed., pp 34-35

[8] http://dictybase.org/techniques/media/media.html#DB, accessed 03/22/2012

[9] R.H. Kessin 2001. Dictyostelium: evolution, cell biology, and the development of multicellularity., Cambridge, Cambridge University Press

[10] J. Franke and R.H. Kessin 1977. Proc. Natl. Acad. Sci. USA. 74:2157-2161

[11] S.-Y. Cheng, S. Heilman, M. Wasserman, S. Archer, M.L. Shulerac and M. Wu 2007. Lab Chip. 7:763-769

[12] S. Kalimuthu and J. Abraham 2009. Biosens. Bioelectron. 24:3575-3580

[13] I.F. Sbalzarini and P. Koumoutsakos 2005. J. Struct. Biol. 151:182-195

[14] P.I.J. Kakebeeke, R.J.W. De Wit and T.M. Konijn 1980. J. Bacteriol. 143:307-312

[15] http://reference.wolfram.com/mathematica/ref/SmoothKernelDistribution.html, accessed 03/22/2012

[16] B. Hu, W. Chen, H. Levine, W.J. Rappel 2011. J. Stat. Phys. 142:1167-1186

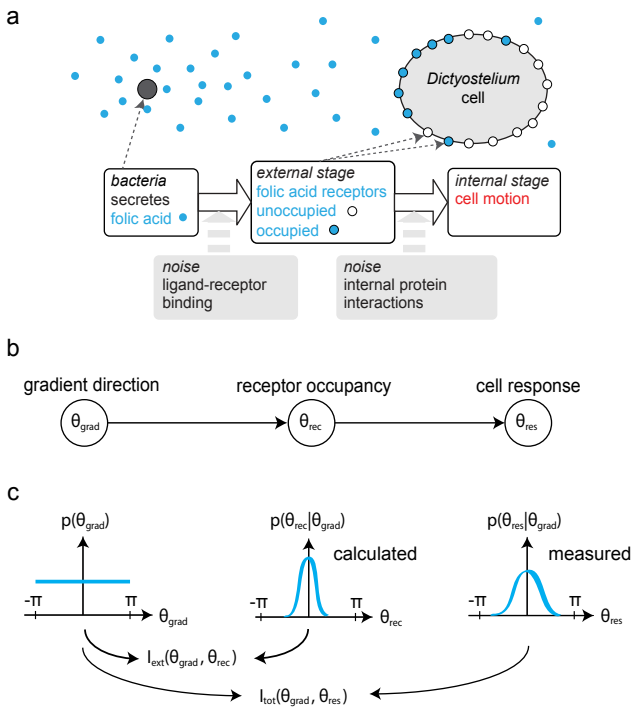

Figure 1: The current paradigm for eukaryotic chemotaxis and the model assumptions. (a) Bacteria secrete folic acid (FA), which then binds to *Dictyostelium* FA receptors. *Dictyostelium* measures spatial distribution of occupied folic acid receptors and these binding events trigger a cascade of intracellular events eventually leading to cell movement. (b) Markov chain model assumption used in our work: the receptor occupancy θ_{rec} depends on the gradient θ_{grad}, and the cell response θ_{res} conditionally depends on the gradient. (c) The external (I_{ext}) and total mutual information (I_{tot}) compared in this work. As detailed in Methods, I_{ext} measures the information gained about the gradient, given the calculated spatial distribution of bound receptors, while I_{tot} measures the information gained given the distribution of cell responses. Assuming the Markov chain relationship in part b), the data processing inequality states $I_{tot} \leq I_{ext}$.

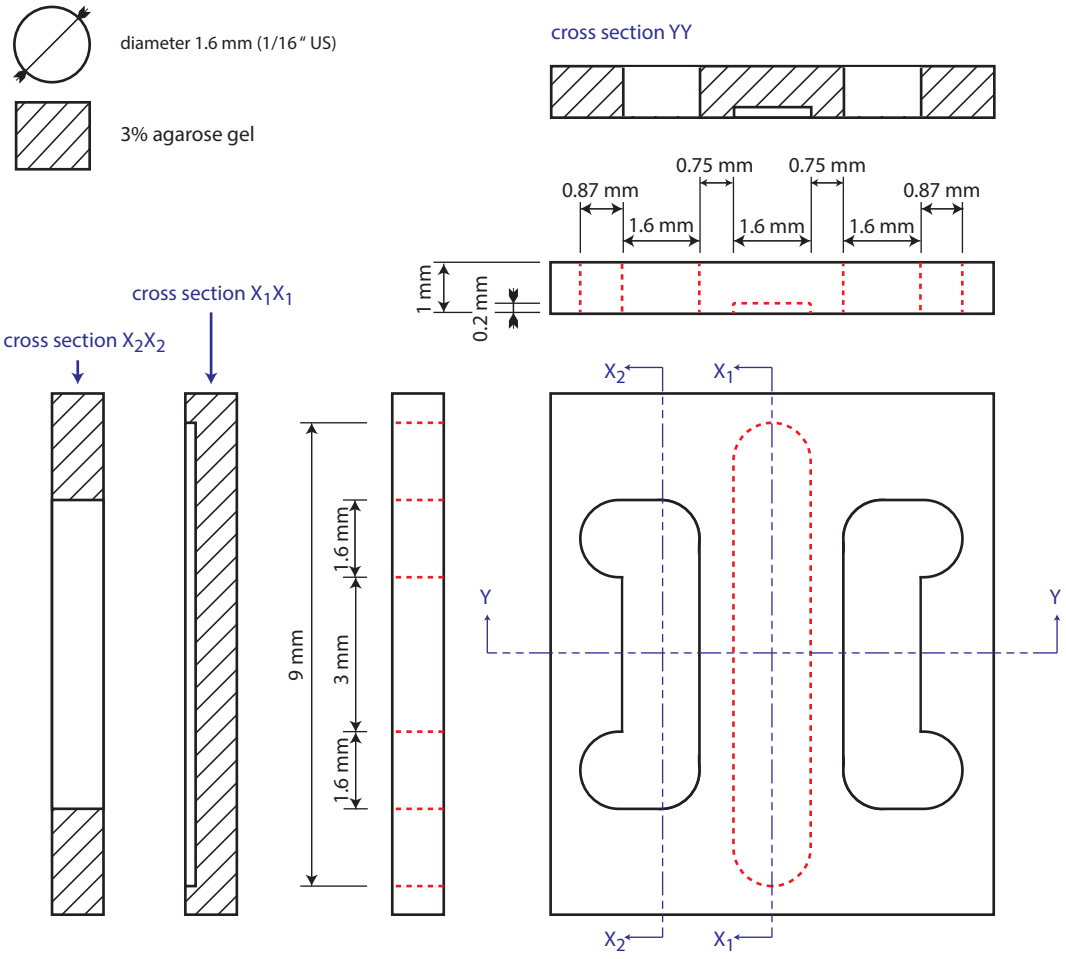

Figure 2: A schematic of the microfluidic device used here.

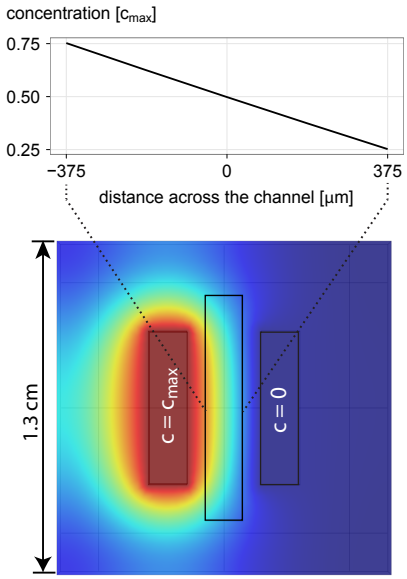

Figure 3: Numerical 2D time-dependent simulation of diffusion through the agarose based microfluidic device used in this work, indicating a steady state gradient in the middle chamber. The top graph shows a FA concentration at the center of the channel 5 hours after the gradient started forming, in units of the FA concentration in the left channel, c_{max} (a slice through the middle of bottom figure). The bottom figure shows a concentration profile intensity of FA at the time of recording, 5 hours after the gradient started forming. Note the steady state has not been formed in the entire device, but only in the middle chamber.

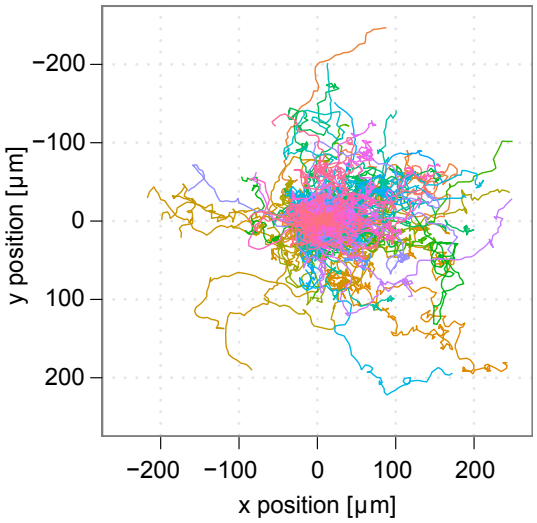

Figure 4: Typical cell trajectories obtained from an experiment with $c_0 = 33\,K_d$ and $dc/dx = 0.11\,K_d/R$ ($K_d = 150\,\mathrm{nM}$). Different colors indicate different cell trajectories.

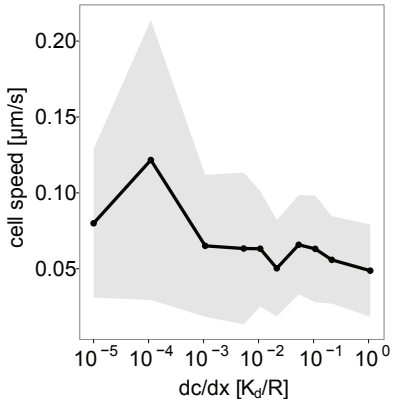

Figure 5: Average and the standard deviation of cell speeds for the experiments given in Fig.1b in the main text. $K_d = 150\,\mathrm{nM}$, $R = 5\,\mu\mathrm{m}$.

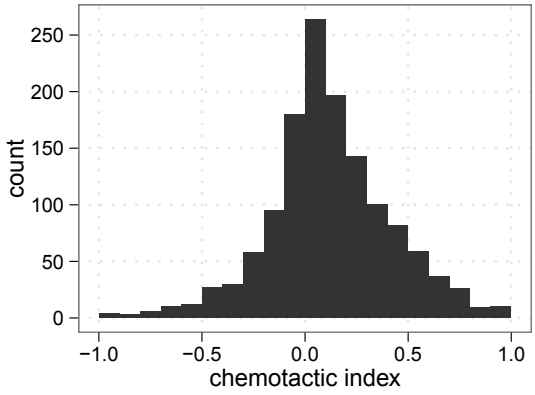

Figure 6: Histogram showing the distribution of chemotactic index for our peak experiments with the mean concentration of $2.5\ \mu\mathrm{M}$ and the gradient of $1.6\ \mathrm{nM}/\mu\mathrm{m}$.

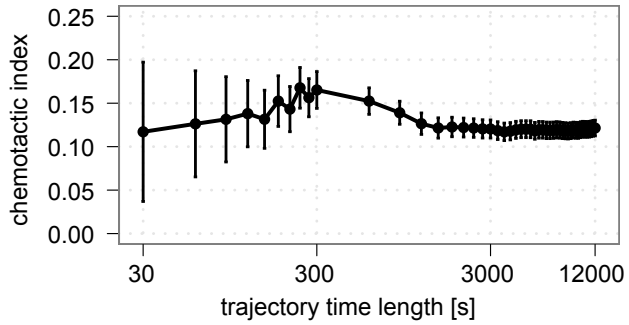

Figure 7: Chemotactic index (CI) as a function of the trajectory time length (or the maximum allowed integration time) for a single representative experimental run with the mean concentration of $2.5\ \mu\mathrm{M}$ and the gradient of $1.6\ \mathrm{nM}/\mu\mathrm{m}$.

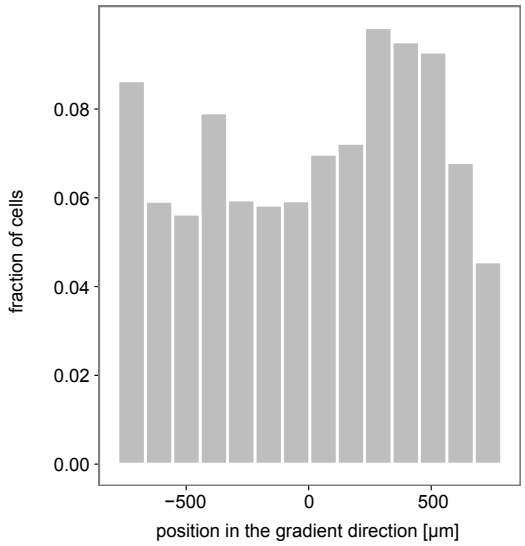

Figure 8: The typical cell distribution as a function of the coordinate in the gradient direction, shown for the experimental run that gave the peak response with $c_0 = 2500\,\mathrm{nM}$ and $dc/dx = 1.6\,\mathrm{nM}/\mu\mathrm{m}$ for $M = 15$ segments.

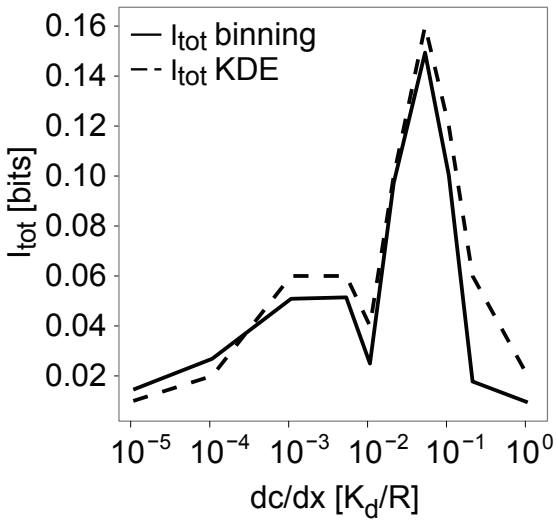

Figure 9: Comparison of two methods for calculating I_{tot}: first binning the data and approximating the integral for I_{tot} with a sum and the second, approximating the discrete data with a continuous function obtained by kernel density estimation [15], showing that both methods give very similar results. Here we used $K_d = 150\,\mathrm{nM}$ and $R = 5\,\mu\mathrm{m}$.

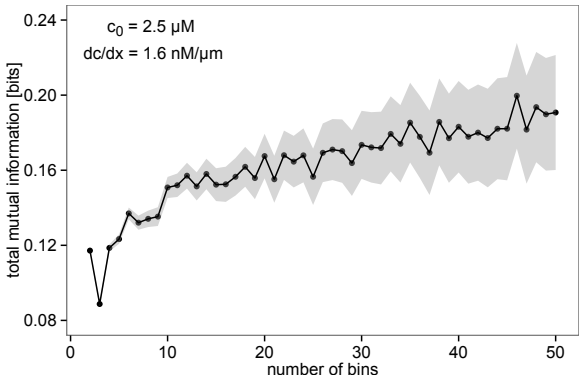

Figure 10: The dependence of the total mutual information I_{tot} on the number of bins for the experiment with $c_0 = 2.5\ \mu\mathrm{M}$ and $dc/dx = 1.6\ \mathrm{nM}/\mu\mathrm{m}$. Shaded area shows the error in estimating I_{tot} according to the ref.[18] in the main text.

Chapter 3

Extracellular amplification of chemical gradients by eukaryotic cells

Igor Segota and Carl Franck

Laboratory of Atomic and Solid State Physics, Cornell University, Ithaca 14853, USA

[in revision for Physical Review Letters]

Abstract

Eukaryotic cells can sense and respond to very shallow chemical gradients by measuring the spatial concentration differences, through the difference in the number of occupied receptors across the cell body. Many kinds of eukaryotic cells secrete enzymes that degrade these chemical signals and affect the local concentration gradient perceived by the cell. Here we analyze this largely ignored effect on gradient sensing, focusing on the important cyclic adenosine monophosphate (cAMP) chemotaxis of starved *Dictyostelium discoideum*, where the cell-secreted cAMP phosphodiesterase (PDE) enzyme degrades cAMP. We model this effect using reaction-diffusion equations which are solved

numerically using a finite element method, for typical experimental microfluidic geometries used in recent work. In contrast to earlier work, we show that realistic concentrations and secretion rates of extracellular PDE can substantially increase the signal-to-noise ratio (SNR) of the occupied receptor difference across the cell body. In addition, our model shows that PDE allows cells to respond to a broader range of cAMP concentrations than would otherwise be possible, as has been qualitatively experimentally observed. Our model also predicts that the optimal cAMP concentration for gradient sensing is always below the cAMP-cAMP receptor dissociation constant K_d, unlike the optimal gradient sensing without PDE which occurs at K_d. Finally, we predict how this extracellular signal processing affects the typically measured chemo-taxis index, allowing for direct experimental tests. A consequence of this model is that many modern microfluidic experiments with flow gradients flush the PDE and therefore disrupt this extracellular part of the signaling pathway, a fact that needs to be taken into consideration.

Key words: Dictyostelium, chemotaxis, cAMP, phosphodiesterase, pdsA-, signal-to-noise, reaction-diffusion, finite element method

1 Introduction

Many eukaryotic cells sense very shallow chemical concentration gradients and direct their motion in the gradient direction in a process called chemo-

taxis. This process is essential for numerous biological functions such as proliferation, organ formation, wiring of the nervous system, wound healing and cancer [1, 2, 3]. In contrast to bacteria [4], eukaryotic cells are large enough ($\gtrsim 10\,\mu$m) to be able to directly measure concentration differences across their bodies [5]. The measurement process is achieved by taking snapshots of the non-uniform occupancy of their cell surface receptors to which diffusing molecules can bind.

The physical limits of chemotactic sensitivity in eukaryotic cells has been extensively studied both theoretically and experimentally, often by calculating theoretical limits and then comparing the accuracy of the experimental chemotaxis response to these limits [5, 6, 7, 8, 9, 10, 11, 12, 13, 14, 15, 16]. For these calculations, it is essential to correctly calculate the local gradient perceived by the cell.

Eukaryotic cells are often found to secrete enzymes that inactivate the chemical signal in the extracellular space, before it binds to its receptor. For example, in *D. discoideum* cyclic adenosine monophosphate (cAMP) chemotaxis, cells secrete cAMP phosphodiesterase (PDE) [17] that hydrolyzes extracellular cAMP [18]. In addition, neutrophils can inactivate chemotactic formylmethionyl peptides [3] and *S. cerevisiae* cells secrete Bar1 protease that degrades α-factor pheromone signals that guide their growth towards their mating partners [19, 20, 21]. More recently, it has been suggested that these enzymes steepen the chemical gradient in *D. discoideum* ([18], p.125) or improve the alignment of the gradient direction with the location of the

nearest mating partner in *S. cerevisiae* [19, 20, 21]. This suggests that these secreted enzymes affect the local gradient in the vicinity of the cell and may provide signal preamplification.

In *D. discoideum*, PDE exists in membrane bound and a secreted extracellular form [22, 23, 24, 25], both encoded by the same gene (*pdsA*). Nanjundiah and Malchow [26] argued, using dimensional analysis, that the extracellular PDE serves no function. More recently, Palsson et al. [27, 28, 29] investigated the role of extracellular PDE in the model of dynamical wave pattern formation and argued that within the particular parameter range of their model, PDE becomes important for wave propagation at low cell densities. Experimentally, *D. discoideum pdsA-* strain has been shown to fail to aggregate [30, 31] and to respond to a reduced range of cAMP concentrations compared to wild-type strains [32]. However, despite these efforts, it remains unclear how the extracellular interaction between cAMP and PDE affects the local concentration gradient perceived by cells.

In this work, we address this question by developing and solving two similar 3D reaction-diffusion models of cAMP-PDE interaction in the extracellular space. First, numerical calculations are done in a typical microfluidic geometry [16, 33], with chemical concentrations fixed on the domain boundaries, while the cell is modeled as a hemispherical cap with fixed PDE flux (Fig.1, SI). Second, we analytically investigate the uniform PDE model, as an approximation of a system with many cells. We use both models to calculate the signal-to-noise ratio of the receptor response following van

Haastert and Postma [34] and using it, predict how the chemotaxis index (a standard quantifier of chemotaxis) is affected by PDE.

2 Fixed PDE secretion rate model

We consider a system of two interacting molecules, PDE and cAMP, following Michaelis-Menten kinetics:

$$\mathrm{PDE} + \mathrm{cAMP} \underset{k_{-1}}{\overset{k_1}{\rightleftharpoons}} \mathrm{COMPLEX} \xrightarrow{k_2} \mathrm{PDE} + 5'\mathrm{AMP} \tag{1}$$

where the COMPLEX represents the intermediate PDE-cAMP complex and 5'AMP the product of this reaction, which does not bind to *D. discoideum* cAMP receptors and acts as a deactivated signal.

The concentrations of cAMP $c(x,t)$, PDE $p(x,t)$, cAMP-PDE complex $C_{cp}(x,t)$ and the 5'AMP $c'(x,t)$, in the standard quasi-steady state assumption [35] (the concentration of the intermediate complex does not change on the time scale of product formation $k_1 cp = (k_{-1} + k_2)C_{cp}$) follow these equations:

$$\begin{aligned}
\frac{\partial c}{\partial t} &= D_c \nabla^2 c - k_1 cp + k_{-1}\frac{cp}{K_M} \\
\frac{\partial p}{\partial t} &= D_p \nabla^2 p \\
\frac{\partial C_{cp}}{\partial t} &= D_{C_{cp}} \nabla^2 C_{cp} \\
\frac{\partial c'}{\partial t} &= D_{c'} \nabla^2 c' + k_2 \frac{cp}{K_M}
\end{aligned}$$

where D_c, D_p, $D_{C_{cp}}$ and $D_{c'}$ are the diffusion constants of cAMP, PDE, cAMP-PDE complex and 5'AMP respectively. Since the cAMP concentration $c\left(\vec{r},t\right)$

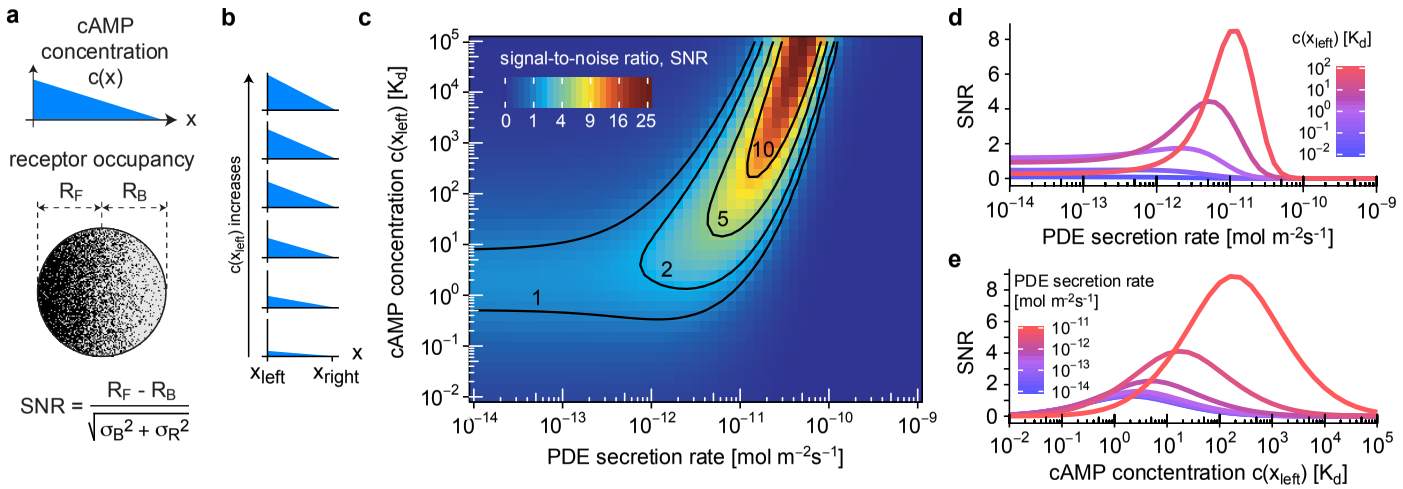

Figure 1: Signal-to-noise ratio (SNR) analysis of the effects of PDE. **a**. SNR is defined as the average receptor difference front-to-back of the cell divided by its statistical uncertainty due to shot noise. **b**. Simulations where the cAMP concentration on the left side $c(x_{\text{left}})$ is varied with $c(x_{\text{right}}) = 0$ (with constant $\nabla c/c = 0.002\,\mu\text{m}^{-1}$) with results shown in parts c,d,e. **c**. SNR as a function of $c(x_{\text{left}})$ and PDE secretion rate (normal flux) p_0 on the cell. **d**.**e**. Horizontal and vertical slices from c. These indicate that increasing PDE secretion rate not only shifts the response towards higher cAMP concentrations (as expected) but can also greatly enhance the SNR.

and PDE concentration $p(\vec{r},t)$ uncouple from the rest of the variables, we omit the other equations. In steady state, we have:

$$D_c\nabla^2 c - \frac{k_2}{K_M}pc = 0 \quad (2)$$

$$D_p\nabla^2 p = 0 \quad (3)$$

and these equations are solved numerically using COMSOL with MATLAB (Comsol Inc.) for the boundary conditiones in Fig.1, SI.

The gradient detection signal-to-noise ratio (SNR) was defined by van Haastert and Postma [34] as (Fig.1a):

$$\mathrm{SNR} = \frac{R_F - R_B}{\sqrt{\sigma_B^2 + \sigma_R^2}} \quad (4)$$

where R_F and R_B are the numbers of occupied receptors at the front half and back part of the cell respectively, σ_R is the receptor noise and σ_B the non-receptor noise. Assuming the steady state of receptor-ligand binding, the numbers of occupied receptors follows the binomial distribution with average and variance:

$$R_{F,B} = \frac{R_T}{2}\frac{c_{F,B}}{c_{F,B}+K_d}, \quad \sigma^2_{R_{F,B}} = \frac{R_T}{2}\frac{c_{F,B}K_d}{(c_{F,B}+K_d)^2} \quad (5)$$

where $c_{F,B}$ are the cAMP concentrations at the front and back half of the cell $c_{F,B} = c\left(x_{\mathrm{cell}} \mp \frac{r}{2}\right)$, K_d is the dissociation constant for the binding between cAMP and cAMP receptors, and R_T is the number of receptors per cell (here $K_d = 30\,\mathrm{nM}$, $R_T = 70,000$ [36]). Since $R_T \gg 1$, we can approximate the binomial distribution of receptor occupancy with normal distribution. Then,

the difference of occupied receptors $\Delta R = R_F - R_B$, is also normally distributed [37]. For reasons to be explained shortly, authors in [34] added the non-receptor noise and time integration to SNR, by adding a constant non-receptor noise σ_B and reducing the receptor variance to $\sigma_R^2 \to \sigma_R^2/I$ where I is the sampling fold (the number of statistically independent measurements of the occupied receptors performed within the given integration time).

The probability "to decipher a cAMP gradient" was defined in [34] as:

$$P_{pos} = P\left(\Delta R > 0\right) - P\left(\Delta R < 0\right) = \mathrm{Erf}\left(\frac{\mathrm{SNR}}{\sqrt{2}}\right)$$

where $\mathrm{Erf}\left(\mathrm{x}\right)$ is the error function. In [34] it was shown that if the fit parameter values $\sigma_B = 25$ and $I = 1.8$ are employed in the definition of SNR, the measured chemotaxis index (CI) strongly correlates with P_{pos}, and follows the following empirical relationship $\mathrm{CI} = P_{pos}(1 - 0.2P_{pos})$, so we have:

$$\mathrm{CI} = \mathrm{Erf}\left(\frac{\mathrm{SNR}}{\sqrt{2}}\right)\left[1 - 0.2\,\mathrm{Erf}\left(\frac{\mathrm{SNR}}{\sqrt{2}}\right)\right] \tag{6}$$

In typical experiments [16, 40, 41], cAMP concentration is changed on the left side of the microfluidic device, while the right side is kept at zero concentration. The parameters used in simulations were: $K_M = 10\,\mu\mathrm{M}$ [38], $D_c = 444\,\mu\mathrm{m}^2\mathrm{s}^{-1}$ [39], $D_p = 70\,\mu\mathrm{m}^2\mathrm{s}^{-1}$, $k_2 = 13,300\,\mathrm{s}^{-1}$(estimated; SI). The results are shown in Figs.1c,d,e and demonstrate the following.

First, secreting PDE can always increase the SNR and can lead up to a factor of 31 increase, from $\mathrm{SNR} = 0.27$ with no PDE to $\mathrm{SNR} = 8.5$ with optimal PDE secretion (Fig.1d). The required PDE secretion rates range

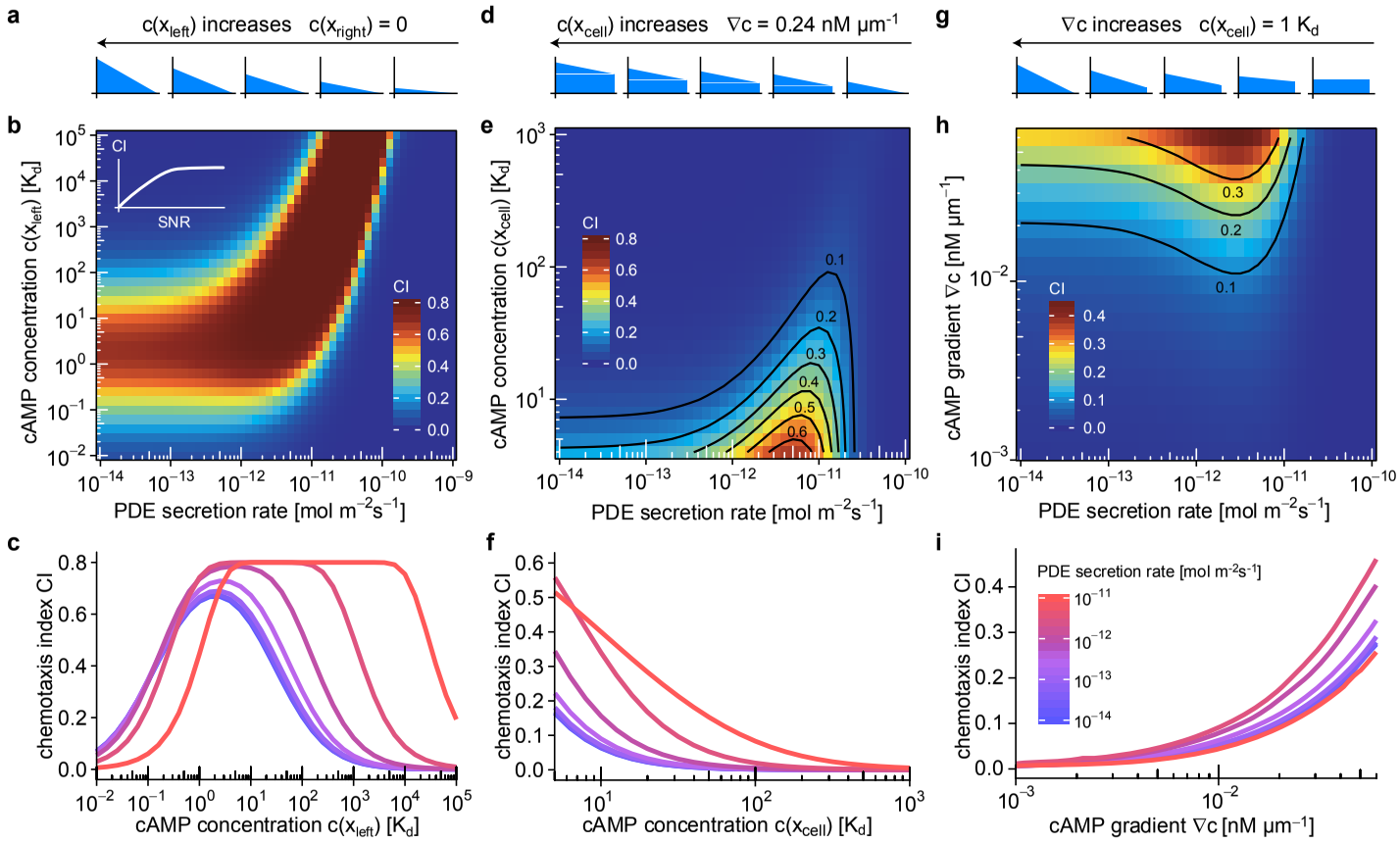

Figure 2: Chemotaxis index, CI for simulations where: **a.b.c.** the cAMP concentration on the left side $c\,(x_{\rm left})$ is changed, while $c\,(x_{\rm right}) = 0.$, **d.e.f.** absolute gradient is fixed at $\nabla c = 0.24\,{\rm nM}\,\mu{\rm m}^{-1}$ and **g.h.i.** the mean concentration in the middle is kept at $c\,(x_{\rm cell}) = 1\,K_d$. The inset in part b shows the dependence of CI on the SNR, following Eq.6. The legend for PDE secretion rates shown in part i applies for parts c,f and i. As discussed in the main text, these predicted changes in the CI can be tested experimentally.

between 10^{-12} and $10^{-10}\,\mathrm{mol\,m^{-2}s^{-1}}$, which falls within the rough physiological range estimated here of $10^{-11}\,\mathrm{mol\,m^{-2}s^{-1}}$ (SI) and by others for Bar1 ($10^{-12}\,\mathrm{mol\,m^{-2}s^{-1}}$), α protease ($10^{-10}\,\mathrm{mol\,m^{-2}s^{-1}}$) and cAMP ($10^{-10}\,\mathrm{mol\,m^{-2}s^{-1}}$) [20, 21, 42].

Second, surprisingly the optimal value of the mean cAMP concentration on the cell is below K_d. In other words, even when we set $c\,(x_{\mathrm{left}}) = 2\,K_d$, which sets the concentration in the middle of the device where the cell is at $1\,K_d$, the SNR can be significantly improved (from $\mathrm{SNR} \approx 0.9$ with no PDE to $\mathrm{SNR}_{\mathrm{max}} \approx 1.6$ for PDE secretion rate $2 \cdot 10^{-12}\,\mathrm{mol\,m^{-2}s^{-1}}$, a 78% increase). The average cAMP concentration on the cell at maximal SNR is $c\,(x_{\mathrm{cell}}) \approx 0.2\,K_d$.

As expected, for zero or very low PDE secretion rates $p_0 \leq 10^{-13}\,\mathrm{mol\,m^{-2}s^{-1}}$, the maximum SNR occurs at the mean cAMP concentration of $c(x_{\mathrm{cell}}) = c(x_{\mathrm{left}})/2 = 1\,K_d$ (Fig.1c,e).

For shallow gradients, low concentrations and dominating receptor noise van Haastert and Postma [34] showed that SNR has a simple analytic expression:

$$\mathrm{SNR} \approx \frac{\Delta c}{\sqrt{c}}\sqrt{\frac{R_T}{16K_d}}\sqrt{I} \tag{7}$$

so we then expect the SNR to scale linearly with the cAMP gradient, and as the inverse square root of the mean cAMP concentration c. This is valid for PDE secretion rates below $10^{-11}\,\mathrm{mol\,m^{-2}s^{-1}}$ (Fig.2c,f, SI).

Using Eq.6 we calculated the changes in CI when either the boundary

concentrations of PDE secretion rate is changed (Fig.2). In the case where $\mathrm{SNR} < 0.7$, $\mathrm{Erf}(\mathrm{SNR}/\sqrt{2}) \approx \sqrt{2/\pi}\mathrm{SNR}$, so the CI is:

$$\mathrm{CI} \approx \sqrt{\frac{2}{\pi}}\frac{\Delta c}{\sqrt{c}}\sqrt{\frac{R_T}{16K_d}}\sqrt{I}$$

which preserves the scaling ($\mathrm{CI} \sim \nabla c$, $\mathrm{CI} \sim c^{-1/2}$).

3 Fixed PDE concentration model

We also consider the model where PDE concentration is time-independent and uniform in space, $p(x,t) = P_0$. Substituting this into the Eq.2, the cAMP concentration equation becomes the diffusion equation with the first order degradation kinetics:

$$\frac{\partial c}{\partial t} = D_c\nabla^2 c - \frac{k_2 P_0}{K_M}c$$

In the steady state this equation is equivalent to the equation for the electrostatic potential with Debye screening [43]. By comparison, in the previous model with constant PDE secretion, the "PDE screening field" was non-uniform in space (Eq. 2). Here, the cAMP concentration can be approximated to depend only on the x direction across the domain, between the two fixed-concentration boundaries (Fig.1, SI). In this case $c(x = -w/2) = c(x_{\mathrm{left}})$, $c(x = w/2) = 0$, the cAMP concentration can be solved analytically:

$$c(x) = c\left(x_{\mathrm{left}}\right)\frac{\sinh\left(\frac{w}{2L} - \frac{x}{L}\right)}{\sinh\left(\frac{w}{L}\right)}, \quad L = \sqrt{\frac{K_M D_c}{k_2 P_0}}$$

When the cell has a radius that is much smaller than the cAMP diffusion characteristic length $r \ll L$ (our case), the SNR defined in Eq.4 in case of

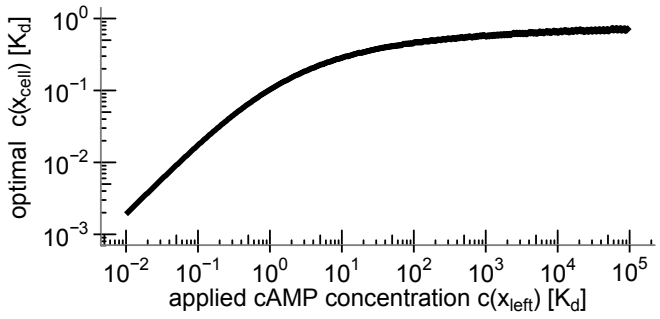

Figure 3: Dependence of the cAMP concentration on the cell $c\left(x_{\text{cell}}\right)$ optimal for gradient sensing, i.e. the one that maximizes the SNR, on the applied cAMP concentration on the left side of the domain $c\left(x_{\text{left}}\right)$. cAMP concentration on the cell in the absence of any PDE is $c\left(x_{\text{cell}}\right) = c\left(x_{\text{left}}\right)/2$. The optimal cAMP concentration on the cell approaches K_d only when the applied concentration is large compared to K_d. When $c\left(x_{\text{left}}\right) = 2\,K_d$, the optimal level of PDE is such that the cell is exposed to the mean concentration of $\approx 0.2\,K_d$ instead of $1\,K_d$.

dominating receptor noise ($\sigma_R \gg \sigma_B$) is:

$$\text{SNR} \approx \frac{\sqrt{R_T}}{2} \frac{\sqrt{K_d}\Delta c}{\sqrt{c}\,(c + K_d)} \sqrt{I} \tag{8}$$

where Δc is the concentration difference between the front $c\left(x = -r/2\right)$ and the back $c\left(x = r/2\right)$ halves of the cell and $c = c\left(x = 0\right)$ is the concentration in the middle of the cell.

In our geometry (Fig.1, SI), the Eq.8 evaluates to:

$$\text{SNR}\left[P_0, c\left(x_{\text{left}}\right)\right] = r\sqrt{I\frac{R_T}{2}\frac{k_2 P_0}{K_M D_c}} \frac{\cosh^{3/2}\left(\frac{w}{2}\sqrt{\frac{k_2 P_0}{K_M D_c}}\right)}{\sinh\left(\frac{w}{2}\sqrt{\frac{k_2 P_0}{K_M D_c}}\right)} \frac{\sqrt{c\left(x_{\text{left}}\right) K_d}}{c\left(x_{\text{left}}\right) + 2K_d \cosh\left(\frac{w}{2}\sqrt{\frac{k_2 P_0}{K_M D_c}}\right)} \tag{9}$$

This analytical expression is first multiplied by a prefactor of 1.45 to correct for the gradient distortion at the cell location due to the presence of the cell (see SI, Section 7) and then plotted in Fig.3, SI. The numerical results

from Fig.1c are therefore also obtained analytically.

As mentioned in the previous model, the optimal PDE levels are never zero, even when the cAMP concentration at the location of the cell is smaller than K_d. The optimal cAMP concentration at the location of the cell after PDE degradation is shown in Fig.3 and approaches K_d only when the cAMP concentration in the absence of PDE would be much greater than K_d.

4 Discussion

In summary, we have investigated the effects of extracellular cAMP phosphodiestarase (PDE) on cAMP gradient sensing in *D. discoideum*. We find that the secretion of PDE by cells shifts their response towards higher cAMP concentrations (as expected) but can also greatly increase the gradient detection signal-to-noise ratio (SNR): up to a factor of 31; Fig.1d. This is in striking contrast to the earlier conclusion reached using dimensional analysis [26]. Furthermore, for any cAMP gradient the cells are exposed to, the optimal PDE secretion rate or concentration for gradient sensing is always greater than zero. Therefore, in contrast to concentration sensing, the optimal gradient sensing occurs at mean cAMP concentration (over the cell) below K_d. As shown in Fig.3, when the mean cAMP concentration on the cell would be K_d in the absence of PDE, the optimal cAMP concentration is around $0.2\,K_d$. The consequences of this model can be experimentally tested as follows.

First, it has been observed that *pdsA*- cells (that do not secrete PDE) respond to the lower range of cAMP concentrations [32], as predicted by our model. These predictions can be tested quantitatively by measuring CI across the entire range of cAMP concentrations as shown in Fig.2, with both wild-type and *pdsA*- cells. It should be noted, however, that *pdsA*- cells lack both the extracellular and membrane-bound form of PDE.

Second, the CI is observed to decrease if the cells are starved for longer time periods, and exposed to the same gradient $\nabla c \approx 3 \times 10^{-2}\,\mathrm{nM}\,\mu\mathrm{m}^{-1}$, $c \approx 30\,\mathrm{nM} = 1\,K_d$ (Fig.4 in [41]). This observation can also be explained by our model. It predicts that the peak response shifts towards higher cAMP concentrations if the PDE accumulates in the environment either as a consequence of higher secretion rate (Fig.2a-c) or longer secretion at a lower secretion rate. More stringent test is to measure the CI across different gradients for cells starved for variable periods of time.

The effects discussed here also lead to different predictions between the experiments with static non-flowing gradients where cAMP gradients are affected by secreted PDE [16, 40, 41] and the experiments with static flowing gradients [13, 11, 14] where the PDE is flushed away. The flow gradient experiments are considered advantageous since the cells are prevented to communicate with each other with cAMP. The flow speeds used in these are around $v = 650\,\mu\mathrm{m/s}$, so based on the Peclet number argument, the advection dominates transports for length scales $L \geq 0.1\,\mu\mathrm{m}$. Even though the speed of the advective flow is such that it does not significantly distort

gradients due to the flow around the cell[44], it still flushes away extracellular PDE. The static gradient experiments do not suffer from this, hence the effect of extracellular PDE needs to be considered.

Finally, it should be noted that this model does not take into account the effects of cAMP phosphodiesterase inhibitor (PDI), which is expected to get secreted later under conditions of high PDE levels [45] and would thereby act to effectively increase the Michaelis-Menten constant of the cAMP-PDE interaction towards millimolar range [38].

Acknowledgments

We thank Cornell ACCEL computer lab for the access to COMSOL Multiphysics and MATLAB software, and anonymous referees for insightful suggestions.

References

[1] K.F. Swaney, C.H. Huang and P.N. Devreotes, "Eukaryotic chemotaxis: a network of signaling pathways controls motility, directional sensing, and polarity", Annu. Rev. Biophys., 39, pp.265-289 (2010)

[2] E.T. Roussos, J.S. Condeelis, A. Patsialou, "Chemotaxis in cancer", Nat. Rev. Cancer, 11, pp.573-578 (2011)

[3] S.H. Zigmond. Ability of polymorphonuclear leukocytes to orient in gradients of chemotactic factors. J. Cell. Biol. 75:606-616 (1977)

[4] V. Sourjik and N.S. Wingreen, "Responding to chemical gradients: bacterial chemotaxis", Curr. Opin. Cell Biol., 24, pp.262-268 (2012)

[5] H.C. Berg and E.M. Purcell, "Physics of chemoreception", Biophys. J., 20, pp.193-215 (1977)

[6] R.G. Endres and N.S. Wingreen, "Accuracy of direct gradient sensing by single cells", PNAS, 105, pp.15749-15754 (2008)

[7] T. Mora and N.S. Wingreen, "Limits of Sensing Temporal Concentration Changes by Single Cells", Phys. Rev. Lett., 104, 248101 (2010)

[8] B. Hu, W. Chen, J-W. Rappel and H. Levine, "Physical Limits on Cellular Sensing of Spatial Gradients", Phys. Rev. Lett., 105, 048104 (2010)

[9] W-J. Rappel and H. Levine, "Receptor noise limitations on chemotactic sensing", PNAS, 105, pp.19270-19275 (2008)

[10] B. Hu, W. Chen, H. Levine and W-J. Rappel, "Quantifying information transmission in eukaryotic gradient sensing and chemotactic response", J. Stat. Phys., 142, pp.1167-1186 (2011)

[11] D. Fuller, W. Chen, M. Adler, A. Groisman, H. Levine, W-J. Rappel and W.F. Loomis, "External and internal constraints on eukaryotic chemotaxis", PNAS, 107, pp.9656-9659 (2010)

[12] M. Ueda and T. Shibata, "Stochastic Signal Processing and Transduction in Chemotactic Response of Eukaryotic Cells", Biophys. J., 93, pp.11-20 (2007)

[13] L. Song, S.M. Nadkarni, H.U. Bodeker, C. Beta, A. Bae, C. Franck, W-J. Rappel, W.F. Loomis and E. Bodenschatz, "Dictyostelium discoideum chemotaxis: threshold for directed motion", Eur. J. Cell Biol., 85, pp.981-989 (2006)

[14] G. Amselem, M. Theves, A. Bae, C. Beta and E. Bodenschatz, "Control parameter description of eukaryotic chemotaxis", Phys. Rev. Lett., 109, 108103 (2012)

[15] G. Amselem, M. Theves, A. Bae, E. Bodenschatz and C. Beta, "A stochastic description of Dictyostelium chemotaxis", PLoS One,7(5):e37213 (2012)

[16] I. Segota, S. Mong, E. Neidich, A. Rachakonda, C. J. Lussenhop and C. Franck, "High fidelity information processing in folic acid chemotaxis of Dictyostelium amoebae", J. R. Soc. Interface, 10, 20130606 (2013)

[17] Y.Y. Chang, "Cyclic AMP phosphodiesterase produced by the slime mold Dictyostelium discoideum", Science, 161, pp.57-59 (1968)

[18] R.H. Kessin, "Dictyostelium: Evolution, Cell Biology and the Development of Multicellularity", Cambridge University Press, Cambridge (2001)

[19] N. Barkai, M.D. Rose, N. Wingreen. "Protease helps yeast find mating partners" Nature 396:422-423 (1998)

[20] S.S. Andrews, N.J. Addy, R. Brent, A.P. Arkin. "Detailed Simulations of Cell Biology with Smoldyn 2.1", PLoS Comp. Biol. 6:e1000705 (2010)

[21] M. Jin, B. Errede, M. Behar, W. Mather, S. Nayak, J. Hasty, H.G. Dohlman, T.C. Elston. "Yeast Dynamically Modify Their Environment to Achieve Better Mating Efficiency." Science Signaling 4: ra54 (2011)

[22] Y.Y. Chang, "Cyclic 3',5'-adenosine monophosphate phosphodiesterase produced by the slime mold *Dictyostelium discoideum*", Science, 161:57-59 (1968)

[23] R.I. Shapiro, J. Franke, E.J. Luna and R.H. Kessin. "A comparison of the membrane-bound and extracellular cyclic AMP phosphodiesterases of *Dictyostelium discoideum*", Biochim. Biophys. Acta, 758:49-57 (1983)

[24] S. Bader, A. Kortholt and P.J.M. van Haastert "Seven Dictyostelium discoideum phosphodiesterases degrade three pools of cAMP and cGMP", Biochem. J., 402:153-161 (2007)

[25] S.J. Orlow, R.I. Shapiro, J. Franke and R.H. Kessin, "The Extracellular Cyclic Nucleotide Phosphodiesterase of Dictyostelium discoideum", J. Biol. Chem., 256, pp.7620-7627 (1981)

[26] V. Nanjundiah and D. Malchow, "A theoretical study of the effects of cyclic AMP phosphodiesterases during aggregation in Dictyostelium", J. Cell Sci., 22, pp.49-58 (1976)

[27] E. Palsson and E.C. Cox, "Origin and evolution of circular waves and spirals in *Dictyostelium discoideum* territories", Proc. Natl. Acad. Sci. USA, 93, pp.1151-1155 (1996)

[28] E. Palsson, K.J. Lee, R.E. Goldstein, J. Franke, R.H. Kessin and E.C. Cox, "Selection for spiral waves in the social amoebae Dictyostelium", Proc. Natl. Acad. Sci. USA, 94, pp.13719-13723 (1997)

[29] E. Palsson, "A cAMP Signaling Model Explains the Benefit of Maintaining Two Forms of Phosphodiesterase in Dictyostelium", Biophys. J., 97, pp.2388–2398 (2009)

[30] J. Barra, P. Barrand, M.H. Blondelet and P. Brachet, "pdsA, a gene involved in the production of active phosphodiesterase during starvation of Dictyostelium discoideum amoebae", Mol. Gen. Genet., 177, pp.607-613 (1980)

[31] R. Sucgang, C.J. Weijer, F. Siegert, J. Franke and R.H. Kessin, "Null mutations of the Dictyostelium cyclic nucleotide phosphodiesterase gene block chemotactic cell movement in developing aggregates", Dev. Biol., 192, pp.181-192 (1997)

[32] G.L. Garcia, E.C. Rericha, C.D. Heger, P.K. Goldsmith and C.A. Parent, "The Group Migration of *Dictyostelium* Cells Is Regulated by Extracellular Chemoattractant Degradation", Mol. Biol. Cell, 20, pp.3295-3304 (2009)

[33] S.-Y. Cheng, S. Heilman, M. Wasserman, S. Archer, M.L. Shulerac and M. Wu. 2007. Lab Chip, 7, pp.763-769

[34] P.J.M. van Haastert and M. Postma, "Biased Random Walk by Stochastic Fluctuations of Chemoattractant-Receptor Interactions at the Lower Limit of Detection", Biophys. J., 93, 1787-1796 (2007)

[35] J.A.M. Borghans, R.J. De Boer and L.A. Segel, "Extending the Quasi-Steady State Approximation by Changing Variables", Bull. of Math. Biology, 58, pp. 43-63, (1996)

[36] R.L. Johnson, P.J.M. van Haastert, A.R. Kimmel, C.L. Saxe III, Bernd Jastorff and P.N. Devreotes, "The Cyclic Nucleotide Specificity of Three cAMP Receptors in Dictyostelium", J. Biol. Chem., 267, 4600-4607 (1992)

[37] E.W. Weisstein, "Normal Difference Distribution", From MathWorld – A Wolfram Web Resource, `http://mathworld.wolfram.com/NormalDifferenceDistribution.html`

[38] R.H. Kessin, S.J. Orlow, R.I. Shapiro and J. Franke, "Binding of inhibitor alters kinetic and physical properties of extracellular cyclic AMP phos-

phodiesterase from Dictyostelium discoideum", Proc. Natl. Acad. Sci. USA, 76, pp. 5450-5454 (1979)

[39] M. Dworkin and K. H. Keller, "Solubility and diffusion coefficient of adenosine 3':5'-monophosphate", J. Biol. Chem., 252, pp.864-865 (1977)

[40] B. Varnum and D.R. Soll, "Effects of cAMP on single cell motility in Dictyostelium", J. Cell Biol., 99, pp. 1151-1155 (1948)

[41] P.R. Fisher, R. Merkl, G. Gerisch, "Quantitative Analysis of Cell Motility and Chemotaxis in *Dictyostelium discoideum* By Using an Image Processing System and a Novel Chemotaxis Chamber Providing Stationary Chemical Gradients", J. Cell Biol., 108, pp.973-984 (1989)

[42] T. Gregor, K. Fujimoto, N. Masaki and S. Sawai, "The Onset of Collective Behavior in Social Amoebae", Science, 328, pp.1021-1025 (2010)

[43] L. Landau, E. Lifshitz, "Statistical Physics Part 1", 1976. 3rd Ed., Pergamon Press, p.241

[44] C. Beta, T. Frohlich, H.U. Bodeker and E. Bodenschatz, "Chemotaxis in microfluidic devices - a study of flow effects", Lab Chip, 8, pp. 1087-1096 (2008)

[45] J. Franke and R.H. Kessin, "The Cyclic Nucleotide Phosphodiesterase Inhibitory Protein of Dictyostelium discoideum", J. Biol. Chem., 256, pp.7628-7637 (1981)

Extracellular amplification of chemical gradients by eukaryotic cells: Supplementary Information

Igor Segota and Carl Franck

Laboratory of Atomic and Solid State Physics, Cornell University, Ithaca 14853, USA

[in revision for Physical Review Letters]

1 Simulation geometry

Here we describe the geometry used for both models (Fig.1a). The boundary conditions for the first, fixed PDE secretion rate model are shown in Fig.1b. As stated in the main text, the second, fixed PDE concentration model has everything the same except zero normal PDE flux on the hemispherical cap.

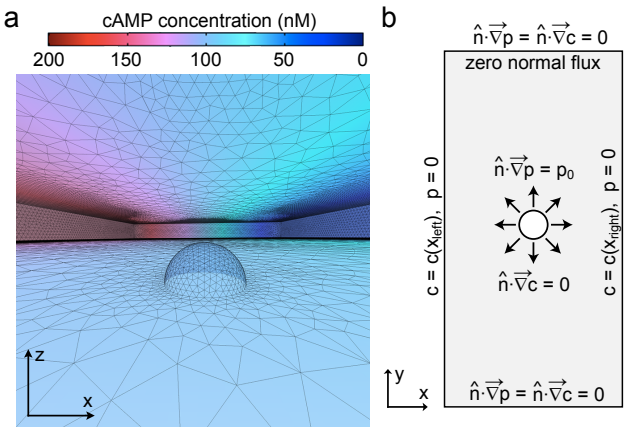

Figure 1: Simulation geometry. **a.** Rectangular domain representing microfluidic device (1mm $\times$ 2mm $\times$ 0.1mm) and a cell modeled as a hemispherical cap (radius 5 μm). cAMP concentration is color-coded, black lines show the intersections of volumetric mesh elements (for the finite element method) with boundaries. **b.** Boundary conditions are fixed concentrations at the sides of the device and zero normal flux (reflective) boundaries at the top and the bottom. The boundary conditions on the hemispherical cap are zero normal flux for cAMP and a constant normal outward flux for PDE. Not shown to scale.

2 Fixed PDE secretion rate model results

We performed simulations where either the absolute gradient ∇c or the mean concentration $c(x_{\text{cell}})$ were held fixed separately. For fixed gradient (Fig.3a), there exists a lower limit on the mean concentration $c(x_{\text{cell}})$ due to the finite width of the microfluidic device, i.e. due to the fact that $c(x_{\text{right}}) \geq 0$, $c(x_{\text{cell}}) \geq w\nabla c/2$. Starting from this mean concentration we show that the SNR can be significantly enhanced, e.g. from 0.3 to 1.2 by increasing the PDE secretion rate to $p_0 \approx 5 \cdot 10^{-12}\,\text{mol}\,\mu\text{m}^{-2}\text{s}^{-1}$(Fig.3b,c). Similarly, if the mean concentration is fixed (Fig.3d), the possible gradients are $\nabla c \leq 2c/w$ and we show these results in Fig.3e,f. Here surprisingly, the PDE secretion rate beyond $p_0 \gtrsim 10^{-12}\,\text{mol}\,\mu\text{m}^{-2}\text{s}^{-1}$ increases the SNR even when concen-

tration is lowered below K_d. This means that PDE could serve to enhance receptor gradient signal even at $c(x_{\text{cell}}) = 1\, K_d$.

3 Fixed PDE concentration model results

Here we show the plot of the analytical solution for the SNR in the case of fixed PDE concentration, Eq.9 from the main text (Fig.2).

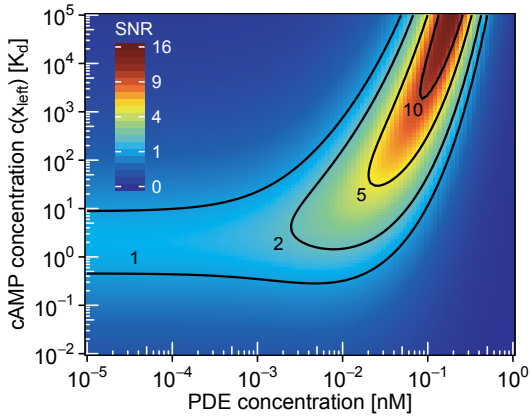

Figure 2: The 2D density plot of the analytical expression for $\text{SNR}\left[P_0, c\left(x_{\text{left}}\right)\right]$ for the model of uniform PDE concentration, Eq.9 in the main text (verified numerically). Again, there is a significant enhancement of the SNR due to the extracellular degradation of cAMP, confirming the results of the previous model presented in Fig.1 of the main text.

4 Estimate of the PDE diffusion coefficient

Diffusion coefficient for PDE was estimated using the Stokes-Einstein equation for spherical particles following the approach by Tyn and Gusek [1, 2], who provided the following equation for globular proteins:

$$D[\text{c}m^2/\text{s}] = \frac{9.2 \cdot 10^{-8} T[\text{K}]}{\eta[\text{mPas}] \cdot (M_r[\text{Da}])^{1/3}}$$

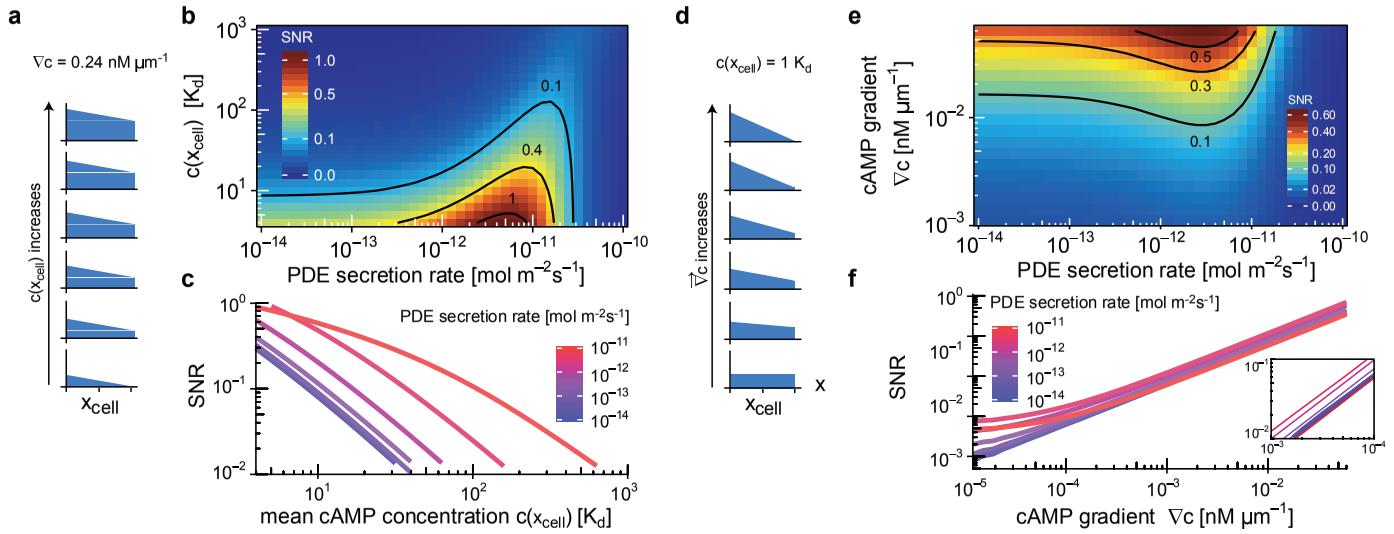

Figure 3: **a**. Simulations where the applied gradient is kept fixed but the mean cAMP concentration $c(x_{\text{cell}})$ is varied; results shown in b,c. **b**.c. SNR as a function of $c(x_{\text{cell}})$ and p_0. Graphs in c are vertical slices from b. **d**. Simulations where the applied mean cAMP concentration is fixed, and the gradient is varied; results shown in e,f. **e**.**f**. SNR as a function of $c(x_{\text{cell}})$ and p_0. Graphs in e are vertical slices from f. In both cases, these simulations show that the SNR is significantly enhanced for physiological secretion rates (10^{-12} to 10^{-11} $\text{mol}\,\text{m}^{-2}\,\text{s}^{-1}$).

where T[K] is the absolute temperature in Kelvins, $\eta_{\text{water}}^{T=293.15K} = 1\,\text{mPas}$ is the dynamic viscosity of water at $20°$C and M_r[Da] molecular mass. The PDE which has a molecular mass $M_r = 57,500$ Da, then has an estimated diffusion rate of $D_p = 70\,\mu\text{m}^2\text{s}^{-1}$.

5 Estimate of the cAMP-PDE turnover number

We estimated the turnover number k_2, from [3, 4] using $k_2 = V_{max}/P_0$, where V_{max} is the maximum rate of 5'AMP production and p is the PDE concentration present. The PDE concentration present in [4] was approximately:

$$P_0 = \frac{n}{V} = \frac{m/M_r}{V} = \frac{6 \cdot 10^{-4} g}{2\,l \cdot 57,500\,g/\text{mol}} \approx \frac{1 \cdot 10^{-8}\,\text{mol}}{2\,l} = 5\,\text{nM}$$

from $8{\cdot}10^{10}$ cells. Therefore, since in [3] authors estimated $V_{max} = 10^{-4}\,\text{M/min}$ from $2 \cdot 10^9$ cells, we estimated that the PDE concentration was proportionally lower: $P_0 = (2 \cdot 10^9\,\text{cells} \cdot 5\,\text{nM})/(8 \cdot 10^{10}\,\text{cells})$ which gives us $P_0 = 0.125\,\text{nM}$. We then used this PDE concentration and V_{max} to estimate the turnover number:

$$k_2 = \frac{V_{max}}{P_0} = 13,300\,\text{s}^{-1}$$

6 Estimate of the PDE secretion rate

In Fig.1 of [5], the slope for the PDE activity gives 100 units/ml, and the text gives 2150 units = 0.31 nmol of PDE, so 1 unit of activity corresponds to $1.44 \cdot 10^{-2}$ nmol of PDE. Therefore the secretion rate for the entire sample

was:

$$\begin{aligned} p_0' &= \frac{1.44 \cdot 10^{1-9}\,\mathrm{mol}/l}{50\,\mathrm{hr}} \cdot 0.7\,l \\ &= 5.6 \cdot 10^{-14}\mathrm{mol\,s^{-1}} \end{aligned}$$

Now we assume the PDE flux is uniform through the entire hemispherical surface of the cell with the radius $5\,\mu\mathrm{m}$, and given the total of $N_C = 2.6 \cdot 10^7$ cells, the PDE secretion rate per cell (expressed as a flux) is:

$$\begin{aligned} p_0 &= \frac{P_0}{2\pi r^2 \cdot N_C} \\ p_0 &= \frac{5.6 \cdot 10^{-14}\mathrm{mol\,s^{-1}}}{2\pi(5\mu\mathrm{m})^2 \cdot 2.6 \cdot 10^7} \\ &= 1.4 \cdot 10^{-11}\mathrm{mol\,m^{-2}s^{-1}} \end{aligned}$$

7 Cell boundary effects on perceived gradients

We estimated the gradient enhancement by a factor of 1.45 is due to the effects of cell shape (i.e. due to the cell modeled as a reflective boundary of hemispherical shape) in the same way as authors in [6] and this effect is shown in Fig. 4.

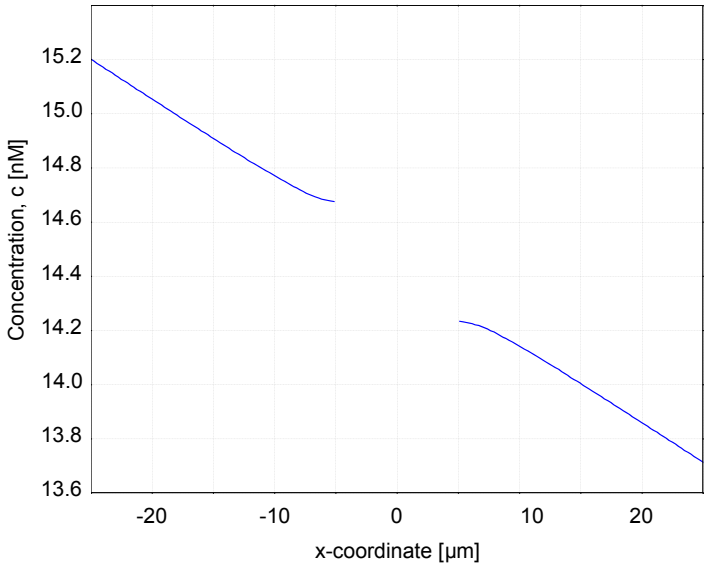

Figure 4: Effect of cell size on the perceived gradient. The actual cAMP concentration, modeled as an insulating boundary is shown as a function of x coordinate, where the hemispherical cap representing the cell extends over $\pm 5 \mu \mathrm{m}$.

References

[1] G. Carta and A. Jungbauer, "Protein Chromatography: Process Development and Scale-Up", Wiley-WCH, p.36 (2010)

[2] M.T. Tyn and T.W. Gusek, "Prediction of Diffusion Coefficients of Proteins", Biotechnol. Bioeng., 35, pp.327-338 (1989)

[3] R.P. Yeh, F.K. Chan and M.B. Coukell, "Independent regulation of the extracellular cyclic AMP phosphodiesterase-inhibitor system and membrane differentiation by exogenous cyclic AMP in *Dictyostelium discoideum*", 66, pp.361-374 (1978)

[4] S.J. Orlow, R.I. Shapiro, J. Franke and R.H. Kessin, "The Extracellular Cyclic Nucleotide Phosphodiesterase of *Dictyostelium discoideum*: Purification and Characterization", J. Biol. Chem., 256, pp.7620-7627 (1981)

[5] J. Franke and R.H. Kessin, "The Cyclic Nucleotide Phosphodiesterase Inhibitory Protein of Dictyostelium discoideum", J. Biol. Chem., 256, pp.7628-7637 (1981)

[6] M. Skoge, M. Adler, A. Groisman, H. Levine, W.F. Loomis and W.-J. Rappel, "Gradient sensing in defined chemotactic fields", Integr. Biol., 2, pp.659-668 (2010)

Chapter 4

Spontaneous emergence of large scale cell cycle synchronization in amoeba colonies

Igor Segota, Laurent Boulet,

David Franck and Carl Franck

Laboratory of Atomic and Solid State Physics,

Cornell University, Ithaca, NY 14853 (USA)

Phys. Biol. 11, 036001 (2014)

Abstract

Unicellular eukaryotic amoebae Dictyostelium discoideum are generally believed to grow in their vegetative state as single cells until starvation, when their collective aspect emerges and they differentiate to form a multicellular slime mold. While major efforts continue to be aimed at their starvation-induced social aspect, our understanding of population dynamics and cell cycle in the vegetative growth phase has remained incomplete. Here we show that cell populations grown on a substrate spontaneously synchronize their cell cycles within several

hours. These collective population-wide cell cycle oscillations span millimeter length scales and can be completely suppressed by washing away putative cell-secreted signals, implying signaling by means of a diffusible growth factor or mitogen. These observations give strong evidence for collective proliferation behavior in the vegetative state.

1 Introduction

Collective oscillations of entire populations characterize many biological processes such as synchronized flashing of fireflies [1], glycolytic oscillations in yeast [2], cell aggregation in amoebae [3], circadian rhythms in cyanobacteria [4], [5], somite segmentation in zebrafish embryos [6], nuclear division in multinuclear HeLa cells [7] and synchronized cleavage divisions in *Xenopus* frog embryos [8]. These cooperative interactions can provide a fitness advantage, e.g. in cases when the environment is depleted of nutrients [3] or to assist in mate finding [1]. Recently, there has been a substantial progress in synthetic biology with the goal of engineering oscillatory genetic networks [9] and coupling them by quorum sensing [10]. In this work, however, the focus is on naturally emergent collective behavior in a model unicellular eukaryote, *Dictyostelium discoideum*. In nature, *D. discoideum* lives in the soil and feeds on bacteria in their vegetative growth state [11]. Keating and Bonner [12] and Kakebeeke et al. [13] showed that vegetative cells can interact by repelling each other and Phillips and Gomer

[14] later identified AprA as an autocrine chemorepellant in vegetative cells. When starved of nutrients D. discoideum transitions to a collective state by chemotactically grouping into multicellular aggregates of 105 cells, eventually differentiating into stalk and spore cells, forming a lifeboat for their genomes. However, in comparison to yeast *S. cerevisiae* [15] or *Xenopus* [16], researchers still do not have a full array of cell cycle markers for *D. discoideum* [17], [18]. The first live-cell S-phase marker has only recently been introduced in *D. discoideum* [19].

2 Results

We studied *D. discoideum* population dynamics on glass substrates. A typical example of the dynamics of the average cell surface density in the exponentially growing regime of the vegetative phase was obtained by automated counting (Fig. 1a). Potentially interesting features are any deviations from pure exponential growth that do not result from uncertainty in counting. Here, the initial cell count is 40 ± 2 cells, spread out uniformly over a 4 mm^2 viewing area. During 26 hours, the cells did not move significantly (200 μm) compared our 2.3 mm by 1.8 mm recording area, resulting in patchy growth (Fig. 1b) further investigated in [20].

First, we show that the deviations from exponential growth (Fig. 1a) indeed represent signatures of collective cell divisions, by measuring the time dynamics of cell size distribution (Fig. 1c). This approach was recently used

to quantify induced cell synchronization [21]. The time dynamics of cell size distributions (Fig. 1c) shows a clear periodic pattern, demonstrating partial synchrony in cell growth. To ensure that this is not a lineage effect (i.e. arising from a low number subpopulation), we show the entire viewing area binned into 27 μm wide squares, with each bin color-coded by the local cell size and averaged over 1-2 cells (Fig. 1d). This demonstrates that synchronization in cell growth is not localized to a particular patch, thereby excluding any possibility of a lineage effect alone causing the large-scale oscillations. The cell-to-cell variation in doubling times is 7.3 ± 0.8 hours (Fig. S4) which is reflected in a strong lineage effect in a monoclonal population (see SI).

Next, we ensured that this periodic growth correlates with cell divisions. We manually annotated all cell division events, omitting initial events corresponding to declustering of cell clusters and cytokinesis of multinuclear cells present in suspension cultures [22], only counting single cell splitting into two, preceded by rounding up at the onset of cytokinesis. These manual annotations agree within 1% to automated counts: for the data presented in Fig. 1, we counted 343 cell division events compared to 344 particles detected by automated counting (excluding initial declustering events). The same was repeated for two other experiments (see Section 3 in the SI). The cell division dynamics shows clear pulses (Fig. 1e) correlated with the beginnings of cell growth pulses (Fig.1c). Furthermore, each collective cell division pulse (colored dots, Fig. 1e) is not localized to a particular patch

(Fig. 1f). However, this still does not exclude the possibility of spontaneous synchronization in suspension cultures which were used to grow cells before plating.

The cells grown in suspensions have a broader size distribution (Fig. 2a) than those on substrates, consistent with previous observations of cell clusters [23] and multinuclear cells [22]. These are all counted as a single particle by automated counting (Fig. 1a), however they are easily discriminated by cell size (particles between 150 and 300 μm^2 in Fig. 1c). Measurements of the cell size distribution dynamics in suspension cultures show no synchronized growth (Fig. 2b), consistent with previous observations in development of D. discoideum synchronization protocols [24] [18] showing no evidence for suspension cell synchronization. Our repeat experiments (see Fig. S1) clearly confirm the onset of synchronization on substrates.

Nevertheless, one might wonder whether this synchronization is an artifact of simultaneous cytokinesis of multinuclear cells and cell cluster disintegration, resulting in a sudden large increase in the number of single cells. Rather, we observed that multinuclear cells undergo cytokinesis and clusters disintegrate uniformly in time throughout the first 6 hours after plating (see supplementary video). This is also reflected in the fact that we do not observe a sudden large increase in the single cell number after the initial incoherent period (Figs. 1 and S1), demonstrating that cell synchronization is not induced by plating. Previous studies in *D. discoideum* have shown that cytokinesis C, which is responsible for cell division of multinuclear cells, is

cell cycle-uncoupled and adhesion-dependent [25], [26], [27], in agreement with our observations.

Next, we investigate the possibility that cells secrete a growth factor or a mitogen that serves as a synchronization signal. We first analyzed the microfluidic experiments we performed previously [23] with cells grown on a substrate in a PDMS microfluidic device (Fig. 2c). In these experiments the cells naturally adhered to the glass while fresh growth medium flowed above them with 0.6, 1.7 and 17 $\mu m/s$ flow speeds. The shear stresses the cells were exposed to in these flowing experiments were at least two orders of magnitude smaller than the shear stresses needed to induce mechanical responses in D. discoideum [28], [29] (for calculation see SI Sec. 7) so it seems unlikely that the loss of coherence is due to the mechanical stress. As discussed later, in subsequent work, on a rare occasion we noticed a few cells advected by flow, presumably as daughters released by mitosis from the substrate. However, this occurred so rarely that it had no effect on our experiments where we had from about 50 to a few hundreds of cells. If the synchronization signal is a small signaling molecule with a diffusion coefficient of about 300 $\mu m^2/s$, then these flow speeds correspond to Peclet numbers (see Section 5, SI), quantifying the ratio of advective to diffusive transport, on the order of 0.35 (diffusion dominated), 1 and 10 (advection dominated), respectively [23]. Again, we measured both the cell density dynamics (Fig. 2d) and the cell size distribution dynamics (Fig. 2e). This qualitatively demonstrates the loss of coherence with increasing flow speed.

However, it does not quantify the degree of collective coherence or measure the population fraction locked into this collective rhythm.

In order to quantify the collective synchronization of N cells, we represented the cell cycle position of cell j as a unit vector in complex plane at angle Θ_j (Fig. 3a). The collective cell cycle oscillations are then represented as N points running around a unit circle. The "order parameter" $z = re^{i\Phi} = \frac{1}{N}\sum_{j=1}^{N} e^{i\Theta_j}$ is a vector of the centroid of these N points whose radius r represents the degree of collective phase coherence and measures the oscillation magnitude of the entire population. If all the cells oscillate in unison, then the points are clustered together resulting in r = 1. For random phased cell oscillations, r is smaller but unlikely to approach zero unless N is very large. To address this, we calculated the average and the standard deviation of r for N randomly phased oscillators (SI).

Since cell growth and division are correlated in *D. discoideum* (comparing Figs. 1d and 1e), we defined the cell cycle phase Θ_j to be proportional to the cell size a_j, i.e. $\Theta_j = 2\pi(a_j - a_{min})/(a_{max} - a_{min})$, with the minimum and maximum cell size approximated from the cell size distributions to be given by $a_{min} = 80\ \mu m^2$ and $a_{max} = 150\ \mu m^2$ (the results are robust with respect to changing limits a_{min} and a_{max}). Hence, the area ratio is $a_{max}/a_{min} = 150/80 \approx 1.88$ which is about a factor of two as expected, since the cells tend to flatten on a glass substrate. If the cells were shaped on a substrate as hemispherical caps then doubling their volume would cause the area to increase by a factor of 1.6. The more flattened out the cells are

the more the volume ratio would approach the surface area ratio, so our result does indicate some degree of flattening, consistent with our microscopic observations. The phase coherence r for the experiment analyzed in Fig. 1 shows periodic oscillations (Fig. 3b) which reflects the fact that the cell size distribution broadens between each collective cell division pulse. The peak-to-peak variation in r is about 0.15, with the observed maxima well above the expected value for an incoherent system of the same number of cells and minimum values corresponding to complete incoherency. However, in other experiments there remained some residual level of coherence at the minima (Figs. S1b and S1d). The oscillations in r are possibly a consequence of the fact that while cell growth and division are coordinated, they are still separate processes and the synchronization signal might be a mitogen pulse that initiates cell division but does not persist throughout the majority of the cell cycle. While the true cell cycle phase is more precisely defined through the appearance of particular sets of cyclin proteins [30], no corresponding live-cell markers are available in D. discoideum. However it is still very unlikely that using the "true" relation for $\Theta_j(a_j)$ would erase all trace of the coherence observed here (Figs. 3b, 3c and S1).

We also calculated the phase coherence for the microfluidic flow experiments described above with AX3 cells and additional ones with AX4 cells in a 50% shorter chamber (see Materials and Methods for details) and again confirm the loss of coherence with increasing flow speed - the phase coherence approaches the values expected for randomly phased oscillators (Fig.

3c). On rare occasions in the high flow regime we noticed cells advected by the flow. Since we observed no dependence of overall proliferation rate on flow rate here or in [23], we do not regard these events as having significance for the phase coherence values presented here. We compared the average phase coherence among experiments performed at different flow rates, and note that on average, phase coherence is higher at lower Peclet numbers (lower flow rates). The experiments were pooled into two groups based on the estimated Peclet numbers: low flow ($Pe \leq 0.35$) and high flow ($Pe \geq 1$). For each individual experiment we calculated the average phase coherence r and the average difference between the phase coherence r and its random-system average rincoherent (averaged over 15-20 hours). As indicated on Figs. 3d,e we performed three low flow experiments and four high flow experiments with three and four data points, respectively. We first compared the average r values between these two groups using a two-tailed Welch Two Sample T-test, and obtained the p-value of 0.02. The same was also done for the difference between instantaneous r and its random-system average $r_{incoherent}$, and here we obtained the p-value of 0.01. Comparison between average values of r and $r_{incoherent}$, and its standard errors of the means for each of the performed experiments at different flow rates is shown in Figs. 3d,e.

3 Discussion

Collective synchronization has been theoretically studied in various versions of the simple Kuramoto model [31], [32], [33]. The solution for the Kuramoto model for finite oscillator number predicts sustained coherence with increasing cell number, consistent with our shorter 25-hour data (Fig. 3b), but inconsistent with our longer 40-hour experiments (Fig. S1). In addition, the observed feature of oscillating phase coherence (even if only in cell size) is not predicted by any of the Kuramoto models. These models assume that the coupling strength scales inversely with the number of oscillators, an assumption which needs to be changed in order to make realistic predictions for this system. Here, at least for short times, we expect that the coupling strength is diffusion limited and independent of cell number. A more appropriate description of the synchronized dynamics presented here would also predict a spatial dependence of phase coherence. The onset of synchronization observed here (Figs. 1c, 3b and S1) occurs within a few hours which is consistent with the approximately 4 hour time needed for a small molecule with a diffusion coefficient of 300 $\mu m^2/s$ to diffuse a distance of 2 mm and thereby cover the entire viewing field.

There is evidence for quorum sensing factors [34], growth factors and factors repressing cell proliferation in *D. discoideum* [35], [36], [37] and their potential role in synchronization remains to be determined. Furthermore, we speculate as to the possible purpose of these oscillations. It is known

that during starvation, *D. discoideum* cells differentiate into prestalk and prespore cells, a process which correlates with cell cycle positions [38], [39], [40]. Since only spore cells potentially survive, there is a competition to form spores. If the cell fate is determined by its cell cycle position (they are certainly correlated), the synchronized fraction could be collectively turned into either prestalk or prespore cells and possibly more effectively competes for becoming spores.

The absence of spontaneously synchronized growth in suspensions might be caused by the fact that the lack of substrate may introduce a stochastic delay of cytokinesis by a time that is difficult to estimate. In addition, the suspension system is further complicated by the fact that cells can cluster [41], grow in 3D and that the presence of shear flow in orbital shakers can affect cytokinesis of multinuclear cells. The cytokinesis pathways are different in suspension and on a substrate (for an overview see [25]). In addition to the lack of oscillations, another difference in culturing cell populations between substrate and suspension growth was the lack of a lag phase on substrates, also previously observed [23]. As reported here, we have not observed any evidence of lagging even when the cells are plated at a very low surface density of around 0.25 cells/mm^2 (see Section 6 in the SI).

As we indicated, these observations are ripe for quantitative modeling and present elegant challenges: macro-scale synchronization of proliferating oscillators where the micro-scale oscillator is the proliferation process itself. Future experimental work will reveal the extent to which this phe-

nomenon is universal. From a practical standpoint, it presents insight into the problem of cell culturing for stem cell development and large scale parallel bioassays where the difficulty of very dilute cell culture arises, as discussed in [23]. It also demands better appreciation of the importance of the nonliving culture environment: flowing suspension vs. hydrophilic substrates with or without fluid flow. Equally interesting are the biochemical circuits in play, e.g. the timing pattern of the chemical signals that cells are apparently exchanging and the biological underpinnings of this process, i.e. how does this synchronization signal affect different phases of the cell cycle and what is the chemical identity of the putative signal molecule responsible for synchronization (based on the Peclet estimates presented here it may well be a small molecule) [42]. Returning to the theoretical challenges, while we have argued that our observations reveal a collective proliferation waves that already encompassed the entire field of view (Fig. 1b and 1d), our understanding of the spatial dynamics of these waves remains an open question.

4 Materials and Methods

Dictyostelium discoideum wild-type AX3 and AX4 axenic strains were grown in HL5 with glucose suspension culture (ForMedium, UK) with 250 μl Pen-Strep (Invitrogen) per 25 ml flask. No variation in results was noticed with cell subculturing for up to one year. Cells were grown in exponential phase

on an orbital shaker (150 rpm) in standard 25 ml Erlenmeyer flasks to 105 or 106 cells/ml (21 C). For substrate growth, these cultures were transferred to fresh HL5, diluted to 103-105 cells/ml and 300 μl samples were plated on hydrophilic MatTek (P50G-1.5-14-F) glass bottom dishes. Recording was performed in bright field with an inverted Olympus IX71 or an upright Nikon Optiphot (4X objective both) within 15 minutes of plating. Images were taken every 5 minutes using a Home Science Tools camera MI-DC5000 or a Logitech QuickCam Pro 4000. The Olympus/Home Science combination provided better resolution (Figs. 1 and S1a) than the Optiphot/Logitech system (Fig. S1c). For suspension growth, flasks ware sampled hourly for 11-12 hours, by injecting a 20 μl sample into a hemocytometer and 20 image sets were taken within 3 minutes.

Background was removed using ImageJ (NIH) by subtracting the average of all images from each frame (for each experiment). Particles were detected and counted using ImageJ by thresholding. Cell sizes were measured using the "Analyze particles" tool. Centroids of particles were used as cell coordinates (Figs. 1c, 1d and 1f). The uncertainty in area measurements is roughly equal to our bin size, i.e. $\pm 10 \mu m$ in Fig.1c.

Microfluidic experiments including imaging systems used were described previously [23]. Briefly, polydimethylsiloxane (PDMS) on glass substrate microfluidic devices (see Fig. 2c, showing a typical configuration for loading exponential phase cells) were employed. The chamber dimensions were 2 mm by 2 mm by 200 μm for AX3 cells and 2 mm by 2 mm by 100 μm

for AX4 cells (these are indicated in Figs. 3d,e as unmarked and asterisk-marked, respectively). After loading, fresh HL5 growth medium was flowed continuously in the direction indicated in the figure. There was no observable difference in behavior between AX3 and AX4 cells. Frames were recorded every 2.5-15 minutes for 16-40 hours. Images were analyzed as described previously. The doubling times were 8-11 hours, consistent with the usual suspension culturing. In an effort to suppress bubble formation in the microchamber, on occasion both HL5 supply and cell suspensions were degassed through rounds of volume increases in closed syringes and mechanical tapping.

5 Acknowledgments

We thank Dicty Stock Center; Northwestern University for AX3 and AX4 cell lines and Cornell Center for Materials Research for use of the facilities funded by the National Science Foundation under grant DMR-1120296.

6 Figures

A list of figures accompanying the main text.

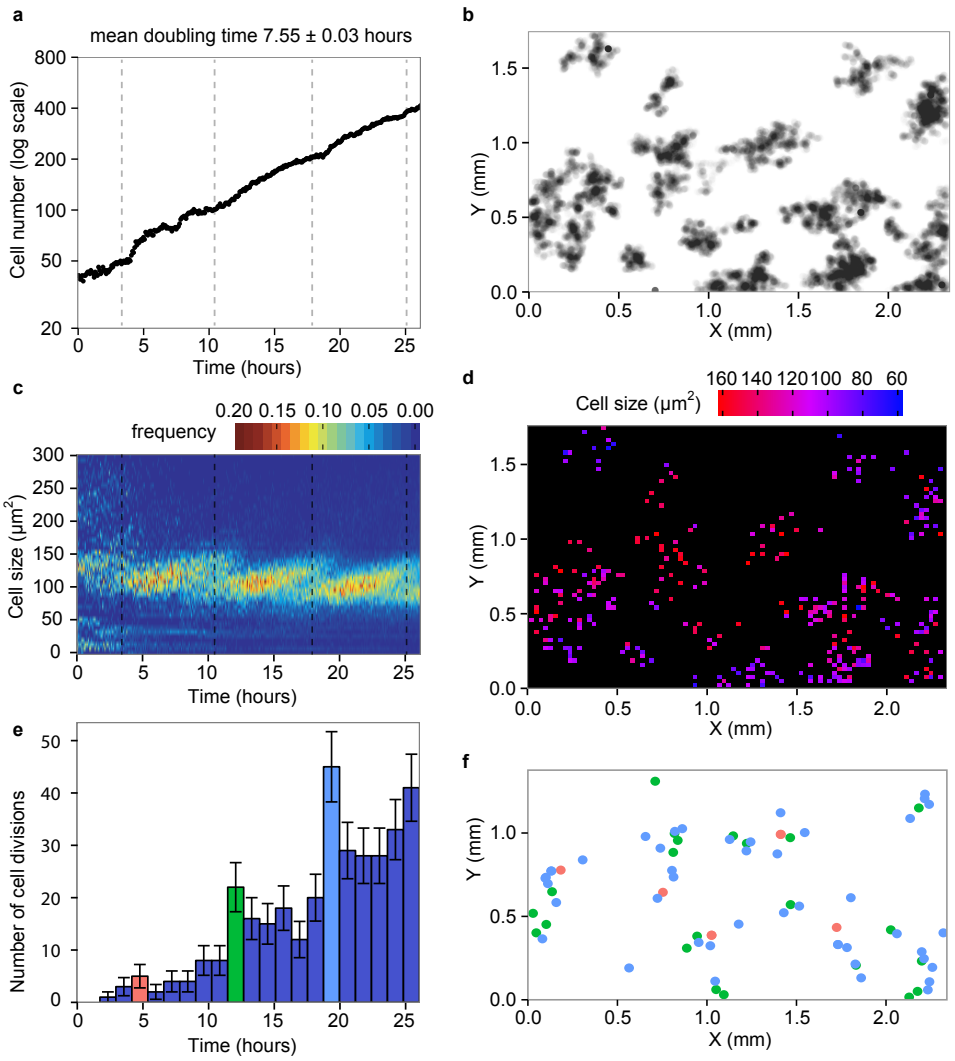

Figure 1: Synchronization of cell growth on a substrate. a, Overall population of proliferating cells vs time showing apparently featureless dynamics b, Strobe (at 5 minute intervals over 26 hours) image of cell positions; darker areas correspond to more visited locations. c, Dynamics of cell size distribution showing clear evidence for cell cycle synchronization after about 4 hours. The sudden jumps are marked by dashed lines, at times also indicated in part a. d, Spatial distribution of cells at 25 hours with color representing cell size. e, Number of cell divisions in 1.2-hour intervals. Peaks in cell divisions correlate with sudden jumps in the cell size distribution shown in part c. Error bars show the upper limit for the counting uncertainty calculated from Poisson noise. f, Spatial distribution of the three cell division peaks from e, with matching colors.

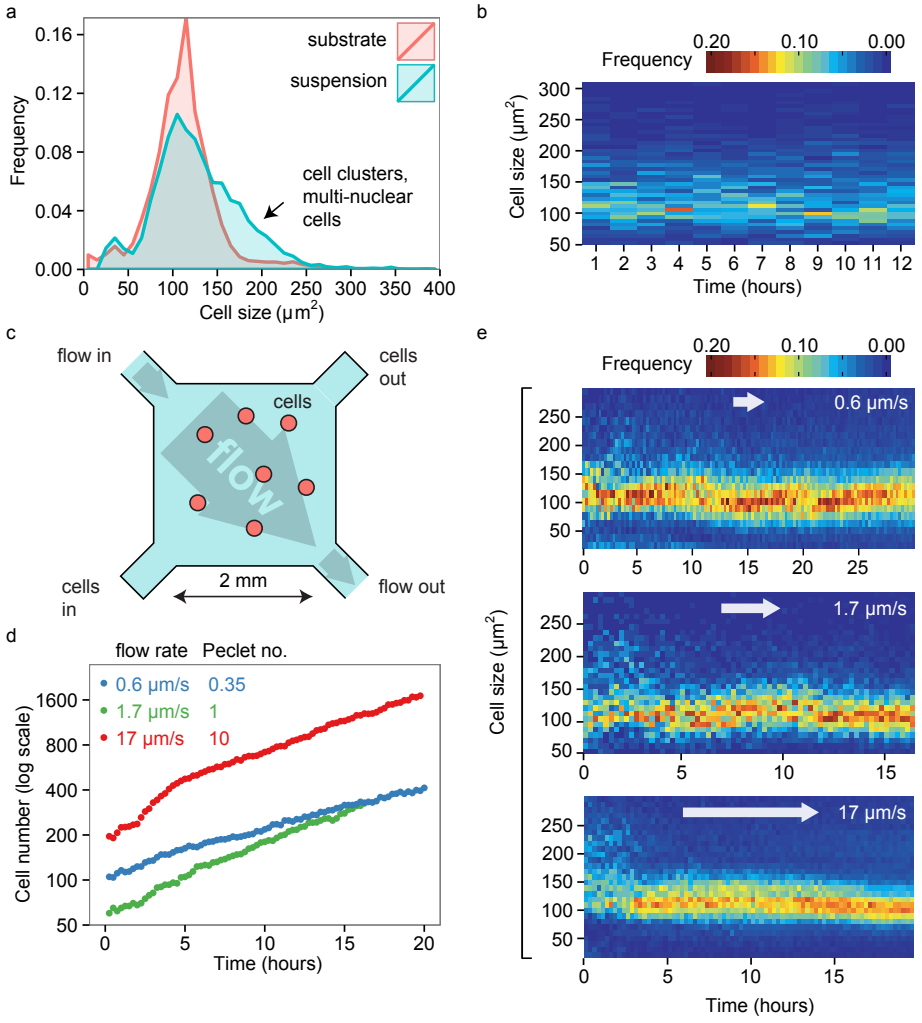

Figure 2: Suspension culture growth and microfluidic flow experiments. a, Time averaged cell size distributions for substrate and suspension growth. b, Time course of cell size distribution in suspension. c, Schematic of the microfluidic device employed for flow experiments. d, Growth dynamics in flow experiments. e, Time course of cell size distributions for substrate flow experiments.

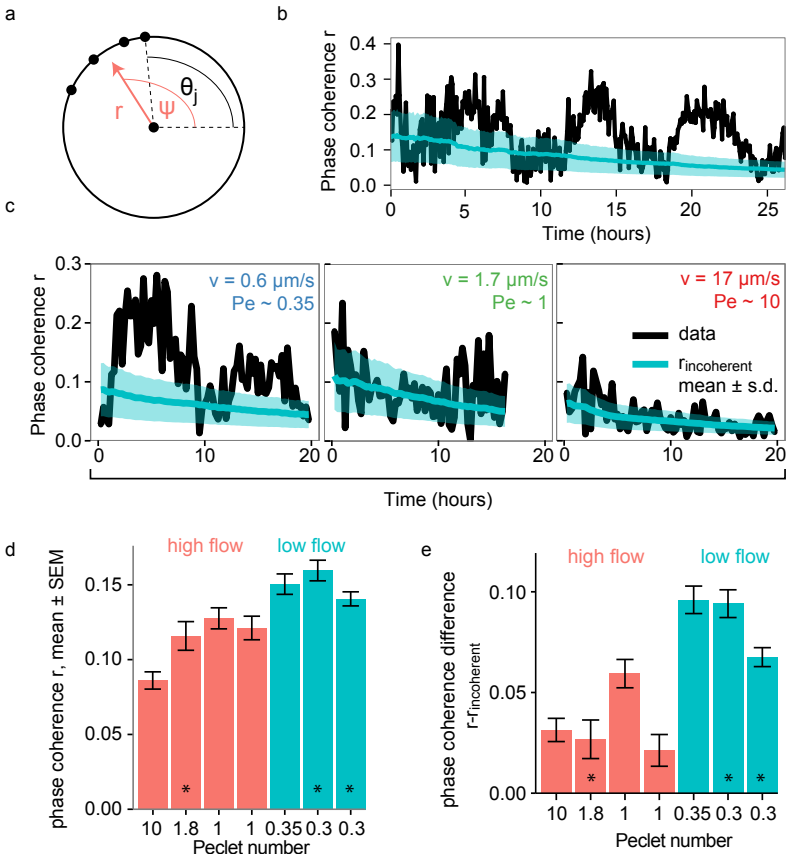

Figure 3: Quantitative analysis of oscillations. a, Phase coherence r, a number between 0 and 1, is defined as a magnitude of the vector sum of N unit vectors each having an angle Θ_j, divided by N (shown in red). The angle Ψ describes the phase of the collective oscillation. b, Phase coherence for the experiment in Fig. 1. The cells periodically go in and out of coherence. c, Phase coherence for microfluidic flow experiments, demonstrating the loss of coherence at higher flow speeds. The cyan line and its spread denote the average and standard deviation for random-phase systems (see Section 1, SI), d,e Phase coherence and its difference from the average for random-phase system as a function of Peclet number (flow rate). Error bars in both d,e, show mean and its standard error. As noted, experiments in d and e were performed either with AX3 cells and 200 μm high microfluidic chamber (unmarked) or AX4 cells and 100 μm high microfluidic chamber (marked with asterisk). The flow rates were adjusted to ensure equal calculated Peclet numbers (Section 5, SI).

7 References

1. Buck, J. and Buck, E., Mechanism of Rhythmic Synchronous Flashing of Fireflies. Science 159, 1319-1327 (1968).

2. De Monte, S., d'Ovidio, F. and Sorensen, P. G., Dynamical quorum sensing: Population density encoded in cellular dynamics. PNAS 104 (47), 18377?18381 (2007).

3. Sawai, S., Thomason, P. A. and Cox, E. C., An autoregulatory circuit for long-range self-organization in Dictyostelium cell populations. Nature 433, 323-326 (2005).

4. Mihalcescu, I., Hsing, W. and Leibler, S., Resilient circadian oscillator revealed in individual cyanobacteria. Nature 430, 81-85 (2004).

5. Yang, Q., Pando, B. F., Dong, G., Golden, S. S. and van Oudenaarden, A., Circadian Gating of the Cell Cycle Revealed in Single Cyanobacterial Cells. Science 327, 1522-1526 (2010).

6. Horikawa, K., Ishimatsu, K., Yoshimoto, E., Kondo, S. and Takeda, H., Noise-resistant and synchronized oscillation of the segmentation clock. Nature 441, 719-723 (2006).

7. Rao, P. N. and Johnson, R. T., Mammalian Cell Fusion: Studies on the Regulation of DNA Synthesis and Mitosis. Nature 225, 159-164 (1970).

8. Kirschner, M., Newport, J. and Gerhart, J., The timing of early developmental events in Xenopus. Trends Genet. 1, 41-47 (1985).

9. Elowitz, M. B. and Leibler, S., A synthetic oscillatory network of transcriptional regulators. Nature 403, 335-338 (2000).

10. Danino, T., Mondragon-Palomino, O., Tsimring, L. and Hasty, J., A synchronized quorum of genetic clocks. Nature 463, 326-330 (2010).

11. Kessin, R. H., Dictyostelium: Evolution, Cell Biology and the Development of Multicellularity (Cambridge University Press, Cambridge, UK, 2001).

12. Keating, M. T. and Bonner, J. T., Negative Chemotaxis in Cellular Slime Molds. J. Bacteriol. 130 (1), 144-147 (1977).

13. Kakebeeke, P. I. J., De Wit, R. J. W., Kohtz, D. S. and Konijn, M. T., Negative chemotaxis in Dictyostelium and Polysphondylium. Exp. Cell Res. 124 (2), 429-433 (1979).

14. Phillips, J. E. and Gomer, R. H., A secreted protein is an endogenous chemorepellant in Dictyostelium discoideum. Proc. Natl. Acad. Sci. USA 109 (27), 10990-10995 (2012).

15. Cai, L. and Tu, B. P., Driving the Cell Cycle Through Metabolism. Annu. Rev. Cell Dev. Biol. 28, 59-87 (2012).

16. Philpott, A. and Yew, R. P., The Xenopus Cell Cycle: An Overview. Mol. Biotechnol. 39, 9-19 (2008).

17. Weeks, G. and Weijer, C. J., The Dictyostelium cell cycle and its relationship to differentiation. FEMS Microbiol. Lett. 124 (2), 123-130 (1994).

18. Weijer, C. J., Duschl, G. and David, C. N., A revision of the Dictyostelium discoideum cell cycle. J. Cell Sci. 70, 111-131 (1984).

19. Muramoto, T. and Chubb, J. R., Live imaging of the Dictyostelium cell cycle reveals widespread S phase during development, a G2 bias in spore differentiation and a premitotic checkpoint. Development 135, 1647-1657 (2008).

20. Houchmandzadeh, B., Neutral Clustering in a Simple Experimental Ecological Community. Phys. Rev. Lett. 101, 078103 (2008).

21. Tzur, A., Kafri, R., LeBleu, V. S., Lahav, G. and Kirschner, M. W., Cell Growth and Size Homeostasis in Proliferating Animal Cells. Science 325, 167-171 (2009).

22. Waddell, D. R., Duffy, K. and Vogel, G., Cytokinesis Is Defective in Dictyostelium Mutants with Altered Phagocytic Recognition, Adhesion, and Vegetative Cell Cohesion Properties. J. Cell Biol. 105, 2293-2300 (1987).

23. Franck, C., Ip, W., Bae, A., Franck, N., Bogart, E. and Le, T. T., Contact-mediated cell-assisted cell proliferation in a model eukaryotic single-cell organism: an explanation for the lag phase in shaken cell culture. Phys Rev E 77, 041905 (2008).

24. Maeda, Y., A New Method for Inducing Synchronous Growth of Dictyostelium discoideum Cells Using Temperature Shifts. Microbiology 132, 1189-1196 (1986).

25. Uyeda, T. Q. P. and Nagasaki, A., Variations on a theme: the many modes of cytokinesis. Curr. Opin. Cell Biol. 16 (1), 55-60 (2004).

26. Hibi, M., Nagasaki, A., Takahashi, M., Yamagishi, A. and Uyeda, T. Q., Dictyostelium discoideum talin A is crucial for myosin OO-independent and adhesion-dependent cytokinesis. J. Muscle Res. Cell Motil. 25, 127-140 (2003).

27. Nagasaki, A., de Hostos, E. and Uyeda, T. Q., Genetic and morphological evidence for two parallel pathways of cell-cycle-coupled cytokinesis in Dictyostelium. J. Cell Sci. 115, 2241-2251 (2002).

28. Fache, S., Dalous, J., Engelund, M., Hansen, C., Chamaraux, F., Fourcade, B., Satre, M., Devreotes, P. and Bruckert, F., Calcium mobilization stimulates Dictyostelium discoideum shear-flow-induced cell motility. J. Cell Sci. 118, 3445-3458 (2005).

29. Decave, E., Rieu, D., Dalous, J., Fache, S., Brechet, Y., Fourcade, B.,

Satre, M. and Bruckert, F., Shear-flow induced motility of Dictyostelium discoideum cells on solid substrate. J. Cell Sci. 116, 4331-4343 (2003).

30. Murray, A. W., Recycling the Cell Cycle: Cyclins Revisited. Cell 116, 221-234 (2004).

31. Kuramoto, Y. and Nishikawa, I., Statistical Macrodynamics of Large Dynamical Systems. Case of a Phase Transition in Oscillator Communities. J. Stat. Phys. 49, 569-605 (1987).

32. Acebron, J. A., Bonilla, L. L., Perez Vicente, C. J., Ritort, F. and Spigler, R., The Kuramoto model: A simple paradigm for synchronization phenomena. Rev. Mod. Phys. 77, 137-185 (2005).

33. Strogatz, S. H., From Kuramoto to Crawford: exploring the onset of synchronization in populations of coupled oscillators. Physica D 143, 1-20 (2000).

34. Gole, L., Riviere, C., Hayakawa, Y. and Rieu, J.-P., A Quorum-Sensing Factor in Vegetative Dictyostelium Discoideum Cells Revealed by Quantitative Migration Analysis. PLoS ONE 6 (11) (2011).

35. Gomer, R. H., Jang, W. and Brazill, D., Cell density sensing and size determination. Develop. Growth Differ. 53, 482-494 (2011).

36. Brock, D. A. and Gomer, R. H., A secreted factor represses cell proliferation in Dictyostelium. Development 132, 4553-4562 (2005).

37. Whitbread, J. A., Sims, M. and Katz, E. R., Evidence for the presence of a growth factor in Dictyostelium discoideum. Dev. Genet. 12, 78-81 (1991).

38. Gomer, R. H. and Firtel, R. A., Cell-Autonomous Determination of Cell-Type Choice in Dictyostelium Development by Cell- Cycle Phase. Science 237, 758-762 (1987).

39. Araki, T., Nakao, H., Takeuchi, I. and Maeda, Y., Cell-cycle-dependent sorting in the development of Dictyostelium cells. Dev. Biol. 162, 221-228 (1994).

40. Wood, S. A., Ammann, R. R., Brock, D. A., Spann, T. and Gomer, R. H., RtoA links initial cell type choice to the cell cycle in Dictyostelium. Development 122, 3677-3685 (1996).

41. Loomis, W. F., The Development Of Dictyostelium Discoideum (Academic Press Inc., New York, p.199, 1982).

42. We thank the anonymous referee for this comment.

43. Swaney, K. F., Huang, C.-H. and Devreotes, P. N., Eukaryotic Chemotaxis: A Network of Signaling Pathways Controls Motility, Directional Sensing and Polarity. Annu. Rev. Biophys. 39, 265-289 (2010).

Spontaneous emergence of large scale cell cycle synchronization in amoeba colonies

Supplementary Information

Igor Segota, Laurent Boulet,

David Franck and Carl Franck

Laboratory of Atomic and Solid State Physics,

Cornell University, Ithaca, NY 14853 (USA)

1 Probability distribution of phase coherence r for N random oscillators

We start by representing the size (area) of each cell by a unit vector with length L=1 in complex plane $e^{i\Theta_j}$ where j is the cell index. The probability distribution of each step is then:

$$p(\vec{r}_j) = \frac{1}{2\pi L}\delta(r_j - L) \tag{1}$$

which is normalized:

$$\int_{\Theta_j=0}^{2\pi}\int_{r_j=0}^{\infty} p(r_j,\Theta_j) r_j dr_j d\Theta_j = \int_{\Theta_j=0}^{2\pi}\int_{r_j=0}^{\infty} \frac{1}{2\pi L}\delta(r_j - L) r_j dr_j d\Theta_j = 1 \tag{2}$$

where $\delta(r_j - L)$ is the Dirac delta function. The average and variance of a single step are:

$$\langle \vec{r}_j \rangle = \int \vec{r}_j p(\vec{r}_j) d\vec{r}_j = 0 \tag{3}$$

$$\sigma_{rj}^2 = \left\langle r_j^2 \right\rangle = \int r_j^2 \frac{\delta(r_j - L)}{2\pi L} 2\pi r_j dr_j = L^2 \tag{4}$$

Also note that:

$$\sigma_{xj}^2 = \frac{1}{2}\sigma_{rj}^2 = \frac{L^2}{2}, \quad \sigma_{rj}^2 = \sigma_{xj}^2 + \sigma_{yj}^2 \tag{5}$$

Now for the average:

$$\vec{z} = \frac{1}{N}\sum_{j=1}^{N} \vec{r}_j,\ z_x = \frac{1}{N}\sum_{j=1}^{N} r_{xj},\ z_y = \frac{1}{N}\sum_{j=1}^{N} r_{yj} \tag{6}$$

we can apply Central Limit Theorem for each x and y component individually (if N is large). Each Cartesian component x and y (of z) then has a Normal distribution with mean 0 and variance $\sigma_{xj}^2/N = L^2/(2N)$. The probability distribution of z is:

$$p(z_x, z_y) = A \exp\left(-\frac{z_x^2}{2\sigma_{xj}^2/N}\right) \exp\left(-\frac{z_y^2}{2\sigma_{yj}^2/N}\right) = A \exp\left(-\frac{r^2}{L^2/N}\right) \tag{7}$$

where the normalization constant can be obtained by requiring that the integral of this probability is 1 and we evaluate the integral in polar coordinates r, Ψ:

$$\int_{\Psi=0}^{2\pi} \int_{r=0}^{\infty} A \exp\left(-\frac{r^2}{L^2/N}\right) r d\Psi dr = 1, \quad A = \frac{N}{\pi L^2} \tag{8}$$

The average phase coherence for a random system can be directly calculated:

$$\langle r \rangle = \int_{\Psi=0}^{2\pi} \int_{r=0}^{\infty} \frac{N}{\pi L^2} \exp\left(-\frac{r^2}{L^2/N}\right) r^3 d\Psi dr = \frac{L^2}{N} \tag{9}$$

so the variance is $\sigma_r^2 = \langle r^2 \rangle - \langle r \rangle^2 = \frac{L^2}{N}\left(1 - \frac{\pi}{4}\right)$ and the standard deviation is:

$$\sigma_r = \frac{L}{\sqrt{N}}\sqrt{\frac{4-\pi}{4}} \tag{10}$$

In Fig.3 in the main text we make use of $\langle r \rangle$ and σ_r to show the average and the standard deviation for the phase coherence for finite populations.

2 Additional examples of cell synchronization

Here we show two more examples indicating an onset of synchronized growth (Fig. S1). The cell synchronization occurs very quickly, within the first several hours. These runs also reveal longer time behavior than in Fig. 3, indicating decay of coherence at long times (see discussion in the main text).

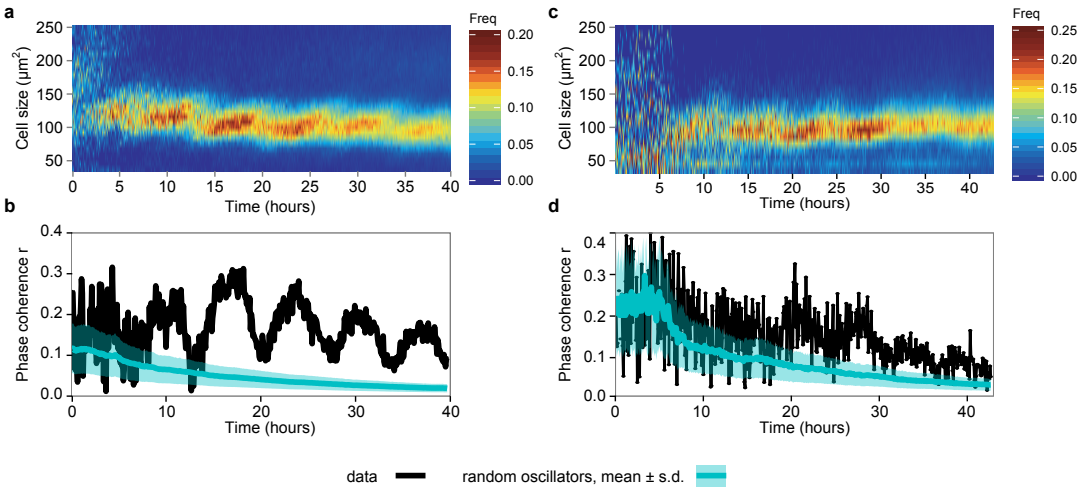

Figure 1: Additional examples of cell synchronization. The dynamics of cell size distribution and phase coherence for the first (a,b) and second (c,d) experiment. As in main text, black lines denote phase coherence in our data and cyan line and its spread shows the mean phase coherence and its spread for the corresponding number of randomly oscillating cells.

3 Statistical analysis of the number of cell divisions vs time

We analyzed the number of cell divisions for three experiments (Fig. S2a) by manually counting each cell division event, as described in the Results section of the main text. The experiments 1 and 3 were performed simultaneously on Olympus IX71 and Nikon Optiphot microscopes in brightfield, as detailed in the Methods section of the main text. Next, these distribution of cell divisions were smoothed using a local polynomial fit [1] (Fig. S2b) and then normalized by the total cell number. The cell densities were 14.5, 10 and 7.4 cells/mm^2, respectively. These smoothed distributions were then divided by the instantaneous cell density at each time point to obtain the relative number of cell divisions over one hour intervals $\Delta N/N$. This is shown in Fig. S3 together with the resulting mean and the corresponding standard error of the mean.

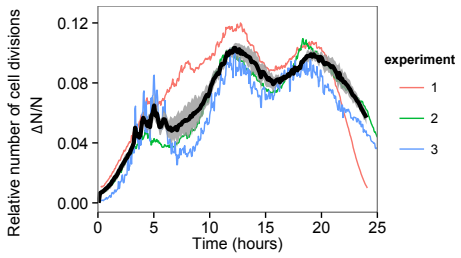

Figure 2: Relative number of cell divisions in one hour time intervals for three experiments (shown in red, green and blue) and its average (black) and standard error of the mean (gray spread).

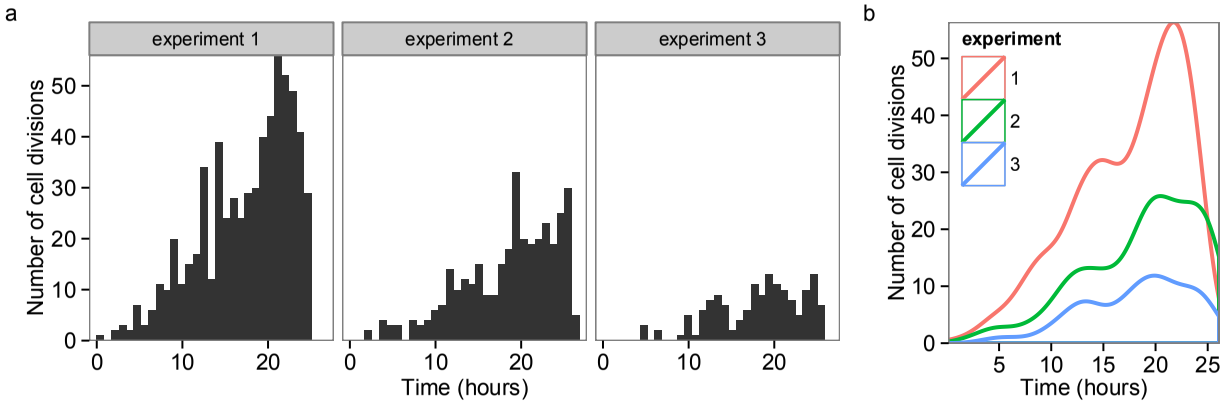

Figure 3: Distribution of cell divisions vs time. a, Histograms showing the number of cell divisions in 1 hour intervals from three different experiments. Experiments 1 and 3 were performed simultaneously. b, Smoothed distributions from a using local polynomial fits [1].

4 Estimate of the variation of the degree of coherence with increasing number of cells

We can estimate of the effect of cell proliferation on the degree of cell cycle synchronization according to the Kuramoto model. Recent efforts to explore the phenomenon of synchronization of many oscillators have focused of extensions of the Kuramoto model to include explicit consideration of network topology, interaction strength and finite population. The problem at hand invites us to consider the last aspect: what are the dynamics of synchronization for a growing population? From [2], we have the following equation for r, long time coherence of the system:

$$r = \sum_{\omega} p(\omega) \left[1 - \left(\frac{\Delta\omega}{Kr} \right)^2 \right]^{1/2} \tag{11}$$

where the summation is over a collection of N oscillators whose unperturbed frequencies are given by the set ?, the probability of each value of frequency is given by $p(\omega)$, K is the interoscillator coupling strength in the (infinitely-ranged) Kuramoto model (Eqn. 1 on p. 146 of [2]) and $\Delta\omega = \omega - \langle\omega\rangle$ is the deviation of the frequency of a particular oscillator from the mean frequency of the entire set of oscillators, $\langle\omega\rangle$. We examine the dependence of r on N with a minimalist distribution: all the oscillators have either $\omega = \omega_0 + \delta$ or $\omega = \omega_0 - \delta$ with equal probability. Then we have the following

equation for r:

$$r = \sum_{\omega} p(\omega) \left[1 - \left(\frac{\delta}{Kr}\right)^2\right]^{1/2} = N\frac{1}{N}\left[1 - \left(\frac{\delta}{Kr}\right)^2\right]^{1/2} = \left[1 - \left(\frac{\delta}{Kr}\right)^2\right]^{1/2} \tag{12}$$

We conclude that r is independent of N. We therefore do not expect the degree of coherence achieved at long times to vary as the cells proliferate.

5 Peclet numbers

Following the discussion in [3] the Peclet number is the dimensionless number quantifying the ratio of advective to diffusive transport, defined as:

$$Pe = \frac{Lv}{D} \tag{13}$$

where L is a characteristic length of the flow cell, v is the advective flow speed and D is the diffusion coefficient of the particle being transported. In our analysis in the main text, we calculated the Peclet numbers for small molecules such as cAMP to give an estimate of the range of flow rates in the microfluidic experiments that could perturb chemical signaling through the intercellular medium.

6 Synchronization in monoclonal populations and lineage effects

We investigated the degree of phase coherence in monoclonal populations, starting from a 1 cell per 4 mm^2 area, which is the minimum cell surface density achievable in our experimental setup. The mean and standard deviation of doubling times owing to cell-to-cell variation were 7.3 ± 0.8 hours. We determined this based on the experiment presented in Fig. 1 in the main text by manually tracking 55 cells (Fig. S4).

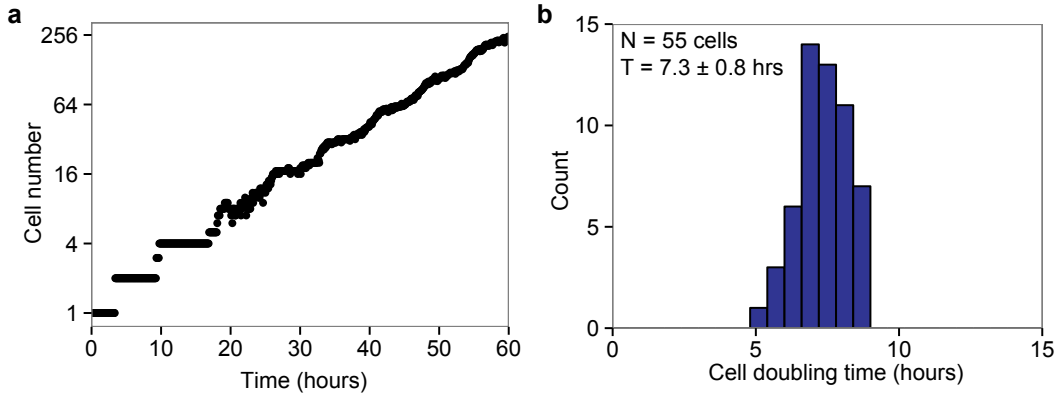

Figure 4: Single cells growth. a, Growth dynamics of single cell growth. b, Distribution of single cell doubling times showing cell-to-cell variability.

If the cell division is thought of as a random walk process with the mean $T_D = 7.3$ hours and standard deviation $\sigma = 0.8$ hours (assuming this is unchanged without coupling), we can estimate the number of generations needed for the complete loss of lineage effect. The number of generations n needed for the standard deviation $\sigma\sqrt{n}$ to become equal to the mean T_D is $n \approx 80$. This is due to the fact that the cell division clock is relatively precise

with only about 10% error (Fig. S4b). The dynamics of cell size distribution and phase coherence for single-cell experiments are shown in Fig. S5 and, as expected, show a very strong lineage effect.

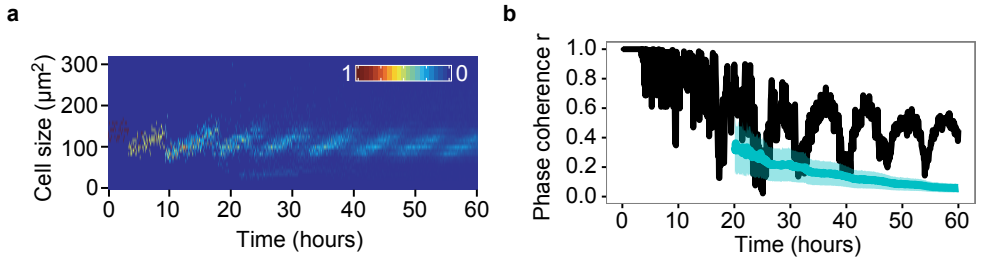

Figure 5: Lineage effects in single cell growth. a, Cell size distribution for a monoclonal population started from a single cell. b, Phase coherence for the same system showing the lineage effect. The cyan line and its spread denote the average and standard deviation for random-phase systems for large number of cells.

7 Shear stresses employed are well below the threshold for cellular response

We consider the shear stress on a cell modeled as a thin planar disk on the bottom of our microfluidic flow chamber. From [4] we expect that such time-independent low Reynolds number (i.e. friction dominated) flow can be approximated as Poiseuille channel flow as follows: We have velocity $u(y)\hat{x}$ in the horizontal (x) direction and velocity variation only along the vertical (y) driven by a constant pressure gradient dP/dx according to:

$$\mu \frac{\partial^2 u}{\partial y^2} = \frac{dP}{dx} \tag{14}$$

where μ is the dynamic viscosity. Applying no slip boundary conditions at the top and bottom of the channel $u(y = 0) = 0$, $u(y = h) = 0$ where h is the height of the channel, gives us the solution for the velocity:

$$u(y) = \left(\frac{dP}{dx}\right)\frac{1}{2}y(y-h) \tag{15}$$

In our case the volumetric flow Q is experimentally fixed so we have (for channel width given by Δz):

$$Q = \Delta z \int_0^h \frac{dP}{dx}\frac{1}{2}y(y-h)dy = -\frac{dP}{dx}\frac{\Delta z \cdot h^3}{12} \tag{16}$$

The shear stress σ in our device near the wall is then (Eq. 1 in [4]):

$$\sigma = \mu\left(\frac{\partial u}{\partial y}\right) = \frac{6Q\mu}{\Delta z \cdot h^2} \tag{17}$$

For our device [3] we have values $\Delta z = 1400\ \mu m$, $h = 200\ \mu m$ and $Q = 0.4\ \mu l/min$ as our maximum flow rate (for Peclet number 10) and we used the dynamic viscosity of water at 25 C, $\mu = 0.894\ mPa \cdot s$ [5]. This gives us a maximum shear stress of $\sigma_{max} = 6.4 \cdot 10^(-4)\ Pa$. Compared to typical shear stresses needed to induce cell motility and rearrangement of actin cytoskeleton in Dictyostelium of about 0.1-0.7 Pa [6] [7], the shear stresses in our experiments are well below these (more than two orders of magnitude). In endothelial cells, the lowest shear stresses needed to induce responses such as potassium channel activation or the rise of intracellular Ca2+ is on the range from $2 \cdot 10^{-2}\ Pa$ to 1 Pa [8]. In the very worst case, the lowest recorded shear stress for these responses in endothelial cells is a factor of 30 greater than the highest shear stress in our experiments [9].

Therefore, it is very unlikely that the loss of cell cycle coherence observed here (Fig. 2e; main text) is due to shear stress.

8 References

1. Available at http://www.inside-r.org/r-doc/stats/loess (2013).

2. van Hemmen, J. L. and Wreszinski, W. F., Lyapunov Function for the Kuramoto Model of Nonlinearly Coupled Oscillators. J. Stat. Phys. 72, 145-166 (1993).

3. Franck, C., Ip, W., Bae, A., Franck, N., Bogart, E. and Thi Le, T., Contact-mediated cell-assisted cell proliferation in a model eukaryotic single-cell organism: an explanation for the lag phase in shaken cell culture. Phys Rev E 77, 041905 (2008).

4. Tritton, D. J., Physical Fluid Dynamics (Oxford University Press, New York, 1988).

5. Dortmund Data Bank, Available at http://www.ddbst.com/en/EED/PCP/VIS_C174.php (2013).

6. Decave, E., Rieu, D., Dalous, J., Fache, S., Brechet, Y., Fourcade, B., Satre, M. and Bruckert, F., Shear-flow induced motility of Dictyostelium discoideum cells on solid substrate. J. Cell Sci. 116, 4331-4343 (2003).

7. Fache, S., Dalous, J., Engelund, M., Hansen, C., Chamaraux, F., Fourcade, B., Satre, M., Devreotes, P. and Bruckert, F., Calcium mobilization stimulates Dictyostelium discoideum shear-flow-induced cell motility. J. Cell Sci. 118, 3445-3458 (2005).

8. Davies, P. F., Flow-mediated endothelial mechanotransduction. Physiol. Rev. 75, 519-560 (1995).

9. Malek, A. M. and Izumo, S., Mechanism of endothelial cell shape change and cytoskeletal remodeling in response to fluid shear stress. J. Cell Sci. 109, 713-726 (1996).

10. De Monte, S., d'Ovidio, F. and Sorensen, P. G., Dynamical quorum sensing: Population density encoded in cellular dynamics. PNAS 104 (47), 18377-18381 (2007).

11. Loomis, W. F., The Development Of Dictyostelium Discoideum (Academic Press Inc., New York, 1982).

Chapter 5

Conclusions

Using the framework of information theory, we found that the fidelity of a model amoeba cell chemotaxis response to folic acid, in fact greatly exceeds its theoretical limit based on the simple receptor-ligand binding model [1,2]. We found that a similar problem may exist in the cAMP chemotaxis as well, as noted in Fig.2 of Chapter 2. We then discussed different modifications to the theoretical model of chemotaxis noise and how they affect the limits of chemical gradient sensing. Therefore, it does not seem that the receptor dynamics can be explained using a simplified model [2] and despite the fact that both cAMP and folic acid receptors share the majority of their signaling pathway, the cell response is qualitatively different as shown by double-peak response in the case of folic acid (Fig.1 in Chapter 2).

One of the main open questions for understanding the receptor limits to chemotaxis is understanding the receptor correlation time. While the current estimates are obtained through numerical simulations [3], there is no supporting experimental data. It is also not clear to what extent the model with N fixed receptors is realistic. In principle, the fact that receptors are diffusing could only reduce the amount of information about the gradient available by the cell (since its position would become more uncertain) but other effects such as receptor turnover (the fact that new receptors can be made by the cell and old degraded) and complicated binding kinetics may play an important role. It is also worth considering whether the appropriate measures of information are in use.

Next, in Chapter 3 we investigated how the cAMP gradient sensing is affected by cell-secreted cAMP phosphodiesterase (PDE), an enzyme that de-

grades cAMP and converts it to inactive 5'AMP. We find that under physiological conditions this enzyme can significantly affect the gradient perceived by cells and that under most conditions greatly amplifies the signal-to-noise ratio of the receptor gradient. The predicitions from our model are very testable experimentally. In the biological arena, there is an opportunity to genetically engineer *D. discoideum* cells where the expression rate of PDE (through the *pdsA* gene) could be controlled experimentally and the chemotaxis response can be measured for varying PDE expression levels. Currently, *pdsA* knockout mutant strains are available [4] and they could be used to compare the chemotaxis response without PDE and with PDE with wildtype cells, since quantiative experiments of this sort are presently still lacking.

Finally, we studied the growth dynamics in the vegetative phase of *D. discoideum* and find that wild-type cell populations grown on a substrate after being transferred from a suspension culture synchronize their cell cycles within several hours [5]. This very surprising result implies that these cells may be engaging in collective behavior even in their vegetative growth phase. This is in stark contrast to the general belief that the vegetative phase is the solitary phase where cells simply feed and divide. As indicated by our microfluidic flow experiments, the synchronization signal seems to be mediated by diffusible molecule, since the degree of coherence decreases as the flow speed is increased. On the experimental front, observations over a large area are needed to measure the characteristic length scale of the phase coherence, since the distant areas are generally not expected to be in synchrony with each other. The technical challenge here is to develop an imaging system that can accurately measure cell areas with the field of view on the order of centimeters squared. Equally important are the currently unknown biochemical circuits involved – it would be

informative to understand how synchronized are different stages of the cell cycle and the chemical identity of the potential signaling molecule (according to our hydrodynamic scaling arguments and our flow experiments its diffusivity is consistent with small molecules, such as cAMP). Since we show that no synchronization occurs in suspension cultures, it is worthwhile to note that upon plating many cells initially undergo cell-cycle independent cytokinesis C events [6]. In these, multinuclear cells divide into multiple uninuclear cells which then synchronize on the substrate. If the cells in the suspension also perform cytokinesis in the cell-cycle independent manner with a stochastic time delay, than this could account for the lack of synchrony observed in suspensions. On the theoretical front, the appropriate description of this system should go beyond the classic Kuramoto model [7], to include the spatial dependence and diffusive transport of the signaling molecule. Our understanding of the spatial dynamics of this synchronization remains an open question. The biological function of this cell cycle synchronization is also unknown but we speculate [5] that it may be relevant in deciding cell fate later during starvation, since the cell fate correlates with the position in the cell cycle [8,9,10].

References

1. I. Segota, S. Mong, E. Neidich, A. Rachakonda, C. J. Lussenhop and C. Franck, High fidelity information processing in folic acid chemotaxis of Dictyostelium amoebae", J. R. Soc. Interface, 10, 20130606 (2013)
2. D. Fuller, W. Chen, M. Adler, A. Groisman, H. Levine, W-J. Rappel and W.F. Loomis, "External and internal con- straints on eukaryotic chemotaxis", PNAS, 107, pp.9656- 9659 (2010)

3. W-J. Rappel and H. Levine, ”Receptor noise limitations on chemotactic sensing”, PNAS, 105, pp.19270-19275 (2008)

4. J. Barra, P. Barrand, M.H. Blondelet and P. Brachet, ”pdsA, a gene involved in the production of active phosphodiesterase during starva- tion of Dictyostelium discoideum amoebae”, Mol. Gen. Genet., 177, pp.607-613 (1980)

5. I. Segota, L. Boulet, D. Franck and C. Franck, ”Spontaneous emergence of large scale cell cycle synchronization in amoeba colonies”, Phys. Biol., 11, 036001 (2014)

6. Uyeda, T. Q. P. and Nagasaki, A., “Variations on a theme: the many modes of cytokinesis.” Curr. Opin. Cell Biol. 16 (1), 55-60 (2004).

7. Kuramoto, Y. and Nishikawa, I., “Statistical Macrodynamics of Large Dynamical Systems. Case of a Phase Transition in Oscillator Communities.” J. Stat. Phys. 49, 569-605 (1987).

8. R.H. Gomer and R.A. Firtel, ”Cell-Autonomous Determination of Cell-Type Choice in Dictyostelium Development by Cell-Cycle Phase”. Science 237, 758-762 (1987).

9. T. Araki, H. Nakao, I. Takeuchi and Y. Maeda, ”Cell-cycle-dependent sorting in the development of Dictyostelium cells.” Dev. Biol. 162, 221-228 (1994).

10. S.A. Wood, R.R. Ammann, D.A. Brock, T. Spann and R.H. Gomer, ”RtoA links initial cell type choice to the cell cycle in Dictyostelium.” Development 122, 3677-3685 (1996).